The ESCRT protein CHMP5 restricts bone formation by controlling endolysosome-mitochondrion-mediated cell senescence

Fan Zhang[1,2,3,#], Yuan Wang[1,2,#], Luyang Zhang[1,2], Chunjie Wang[1,2], Deping Chen[4], Haibo Liu[5], Ren Xu[6], Cole M. Haynes[5], Jae-Hyuck Shim[7], Xianpeng Ge[1,2]

[1]Xuanwu Hospital Capital Medical University, Beijing, China;

[2]National Clinical Research Center for Geriatric Diseases, Beijing, China;

[3]Joint Therapeutics Co. Ltd., Beijing, China;

[4]Beijing Citident Hospital of Stomatology, Beijing, China;

[5]Department of Molecular, Cell and Cancer Biology, University of Massachusetts Chan Medical School, Worcester, Massachusetts, USA;

[6]The First Affiliated Hospital of Xiamen University-ICMRS Collaborating Center for Skeletal Stem Cells, State Key Laboratory of Cellular Stress Biology, Faculty of Medicine and Life Sciences, School of Medicine, Xiamen University, Xiamen, China;

[7]Department of Medicine/Division of Rheumatology, University of Massachusetts Chan Medical School, Worcester, Massachusetts, USA;

[#]These authors contributed equally to this work.

Correspondence to Xianpeng Ge or Jae-Hyuck Shim

Email: xianpeng.ge@xwhosp.org, xpge@penggegroup.com

or Jaehyuck.shim@umassmed.edu

Abstract

The dysfunction of the cellular endolysosomal pathway, such as in lysosomal storage diseases, can cause severe musculoskeletal disorders. However, how endolysosomal dysfunction causes musculoskeletal abnormalities remains poorly understood, limiting therapeutic options. Here, we report that CHMP5, a member of the endosomal sorting complex required for transport (ESCRT)-III protein family, is essential to maintain the endolysosomal pathway and regulate bone formation in osteogenic lineage cells. Genetic ablation of *Chmp5* in mouse osteogenic cells increases bone formation in vivo and in vitro. Mechanistically, *Chmp5* deletion causes endolysosomal dysfunction by decreasing the VPS4A protein, and CHMP5 overexpression is sufficient to increase the VPS4A protein. Subsequently, endolysosomal dysfunction disturbs mitochondrial functions and increases mitochondrial ROS, ultimately resulting in skeletal cell senescence. Senescent skeletal cells cause abnormal bone formation by combining cell-autonomous and paracrine actions. Importantly, elimination of senescent cells using senolytic drugs can alleviate musculoskeletal abnormalities in *Chmp5* conditional knockout mice. Therefore, our results show that cell senescence represents an underpinning mechanism and a therapeutic target for musculoskeletal disorders caused by the aberrant endolysosomal pathway. These results also uncover the function and mechanism of CHMP5 in the regulation of cell senescence by affecting the endolysosomal-mitochondrial pathway.

The endosomal sorting complex required for transport (ESCRT) machinery is an evolutionarily conserved molecular mechanism essential for diverse cell biological processes. Since it was initially discovered in the early 21st century in the budding yeast *Saccharomyces cerevisiae*, the molecular gear has been extensively dissected in the endocytic pathway, which sorts ubiquitinated membrane proteins and bound cargoes that commit to lysosomal degradation [1-4]. In addition to the endocytic process, ESCRT proteins also play critical roles in other cell activities, such as exocytosis, viral budding, cytokinesis, pruning of neurons, repair of the plasma membrane, and assembly of the nuclear envelope [2, 4]. In the endocytic pathway, the ESCRT machinery consists of a series of functionally overlapping protein complexes, including ESCRT-0, -I, -II and -III. While the ESCRT-0, -I, and -II complexes are mainly responsible for protein sorting and recruiting ESCRT-III components, the ESCRT-III complex, cooperating with the ATPase VPS4, is the primary executor of membrane severing during the formation of multivesicular bodies (MVB) [3, 5], which ultimately fuse with the lysosomes for cargo degradation or with the plasma membrane to release cargos into the extracellular space.

Charged multivesicular body protein 5 (CHMP5), the mammalian ortholog of yeast VPS60/MOS10, is a component of the ESCRT-III protein complex and plays an essential role in the late stage of MVB formation [6]. As the yeast *Vps60/Mos10*-null mutation disturbs the endosome-to-vacuole (the lysosome-like structure in yeast) trafficking and affects the sorting of internalized endocytic markers [7], ablation of *Chmp5* in mouse embryonic fibroblasts (MEFs) also affects the sorting from late endosomes/MVBs to lysosomes and reduces lysosomal degradation of multiple activated receptors [6]. Notably, in mouse osteoclasts, CHMP5 suppresses ubiquitylation of the IκBα protein and restricts the activity of NFκB pathway, without

63 any effect on endolysosomal functions [8]. During αβ T lymphocyte development, CHMP5
64 promotes thymocyte survival by stabilizing the pro-survival protein of Bcl2 and does not have an
65 influence on the endolysosomal system [9]. These studies suggest that the regulation of the
66 endolysosomal pathway by CHMP5 depends on the cell and tissue context.
67
68 The dysfunction of the endolysosomal pathway can cause severe musculoskeletal disorders.
69 A such example is lysosomal storge diseases, which include more than 50 different subgroups
70 of diseases due to mutations in genes that encode lysosomal hydrolases or genes that are
71 responsible for the transport, maturation, and functions of lysosomal hydrolases [10].
72 Musculoskeletal pathologies, such as joint stiffness/contracture, bone deformation, muscular
73 atrophy, short stature, and decreased mobility, are among the most common, in some cases the
74 earliest, clinical presentations of lysosomal storage diseases [11, 12]. These musculoskeletal
75 lesions are particularly refractory to current treatments for lysosomal storage diseases, including
76 enzyme replacement treatment and hematopoietic stem cell transplantation [13]. Therefore,
77 studies on the mechanisms of musculoskeletal pathologies due to endolysosomal dysfunction
78 are paramount to design and develop novel treatments for these disorders.
79
80 In this study, our results uncover the function and mechanism of CHMP5 in the regulation
81 of cell senescence and bone formation in osteogenic cells. Deletion of *Chmp5* causes
82 endolysosomal dysfunction involving decreased VPS4A protein and subsequently activates cell
83 senescence by increasing intracellular mitochondrial ROS. Senescent cells induce bone
84 formation in both autonomous and paracrine ways. Importantly, senolytic treatment is effective
85 in mitigating musculoskeletal pathologies caused by *Chmp5* deletion.

86 ## Results

87 ### Ablation of *Chmp5* in mouse osteogenic lineage cells causes aberrant
88 bone formation

89 In addition to the well-characterized role of the CTSK gene in osteoclasts, this gene has
90 recently been reported to identify periskeletal progenitors [14-16]. In particular, the
91 ablation of *Chmp5* in mouse *Ctsk*-expressing cells (hereafter referred to as $Chmp5^{Ctsk}$
92 mice, homozygous) caused dramatic periskeletal bone overgrowth near the joint
93 compared to $Chmp5^{Ctsk/+}$ (heterozygous) and $Chmp5^{fl/fl}$ littermate controls (**Fig. 1A and**
94 **B**). Aberrant periskeletal bone growth in $Chmp5^{Ctsk}$ mice became distinct around
95 postnatal day 10 (d10), progressed with age, and involved multiple bones and joints
96 throughout the body, including knee, ankle, and foot joints (**Fig. 1A to C** and **Fig. S1A**).
97 With age, these animals developed severe skeletal deformities, progressive joint stiffness,
98 reduced motility, and short stature. Despite bone overgrowth in $Chmp5^{Ctsk}$ animals,
99 mechanical tests showed that bone stiffness and fracture stress decreased significantly
100 (**Fig. 1D**), suggesting that bone mechanical properties were impaired in $Chmp5^{Ctsk}$ mice.
101

102 To track $CTSK^+$ periskeletal progenitors during the bone overgrowth in $Chmp5^{Ctsk}$
103 mice, we crossed *Ctsk-Cre*, $Chmp5^{fl/fl}$, and $Rosa26^{mTmG}$ mice to generate
104 $Chmp5^{Ctsk/+};Rosa26^{mTmG/+}$ and $Chmp5^{Ctsk};Rosa26^{mTmG/+}$ reporter animals, in which
105 $CTSK^+$ periskeletal progenitors and their descendants express membrane-localized
106 green fluorescence protein (GFP). In $Chmp5^{Ctsk/+};Rosa26^{mTmG/+}$ control mice, GFP^+ cells
107 could be detected in the perichondrium, groove of Ranvier, periosteum, ligament, and
108 enthesis in addition to osteoclasts in the bone marrow, but not in growth plate

109 chondrocytes (**Fig. 1E**). With *Chmp5* deletion, GFP^{+} cells consisted of a major part of
110 cells in periskeletal overgrowth in *Chmp5*^{Ctsk}*;Rosa26*$^{mTmG/+}$ mice (**Fig. 1E** and **Fig. S1B**).
111 Tartarate resistant acid phosphatase (TRAP) staining did not show TRAP^{+} osteoclasts in
112 the periskeletal lesion, while obvious TRAP^{+} osteoclasts could be detected in the bone
113 marrow (**Fig. S1C**). These results indicate that *Chmp5*-deficient periskeletal progenitors
114 directly contribute to the bone overgrowth in *Chmp5*^{Ctsk} mice.
115
116 Next, we sought to confirm the role of CHMP5 in the regulation of bone formation by
117 deleting this gene using another mouse line of osteogenic lineage Cre. We crossed
118 *Chmp5*$^{fl/fl}$ mice with the line of *Prrx1*-Cre [17], *Col2*-Cre [18] or *Osx*-Cre [19] mice to delete
119 the *Chmp5* gene in *Prrx1*-expressing limb mesenchymal progenitors (*Chmp5*^{Prrx1} mice),
120 *Col2*-expressing perichondral progenitors (*Chmp5*^{Col2} mice) or *Osx*-expressing
121 osteoprogenitors (*Chmp5*^{Osx} mice) and were unable to obtain postnatal homozygous
122 gene knockout mice, probably due to embryonic lethality after ablating C*hmp5* expression
123 in these osteogenic lineages. Subsequently, we used the *Dmp1*-Cre mouse line that could
124 target postnatal endosteal osteoprogenitors, preosteoblasts, mature osteoblasts, and
125 osteocytes [20-22]. *Chmp5*^{Dmp1} mice were born in normal Mendelian ratios and were
126 viable. Within three weeks of age, the skeletons of *Chmp5*^{Dmp1} mice began to show a
127 distinct expansion in comparison with *Chmp5*$^{Dmp1/+}$ and *Chmp5*$^{fl/fl}$ littermate controls,
128 which progressed with age and became much more severe at 1 year of age (**Fig. 1F**).
129 Bone expansion in *Chmp5*^{Dmp1} mice that occurred mainly in the endosteum was further
130 shown in detail around the age of 10 weeks by micro-CT and histological analyses (**Fig.
131 1G** and **Fig. S1D, E**).

132

133 Meanwhile, since *Dmp1*-expressing lineage cells also generate skeletal muscle cells
134 [21], *Chmp5*^{Dmp1} mice showed a profound decrease in skeletal muscle mass with age
135 (**Fig. 1F and H**). Hindlimb abduction, full-limb hanging time, and front-limb pull strength
136 tests showed that muscular functions also decreased profoundly in *Chmp5*^{Dmp1} compared
137 to *Chmp5*$^{fl/fl}$ mice (**Fig. 1I and J**).

138

139 CHMP5 restricts osteogenesis in skeletal progenitor cells

140 To further characterize the function of CHMP5 in the regulation of bone formation, we
141 cultured and sorted *Ctsk*-expressing periskeletal progenitor cells (CD45$^-$;CD31$^-$;GFP$^+$)
142 from periskeletal tissues of *Chmp5*$^{Ctsk/+}$*;Rosa26*$^{mTmG/+}$ and *Chmp5*^{Ctsk}*;Rosa26*$^{mTmG/+}$ mice
143 in the early stage of skeletal lesions (P10-P14) (**Fig. 2A and Fig. S2A, B**, hereafter
144 referred to as *Chmp5*$^{Ctsk/+}$ and *Chmp5*^{Ctsk} periskeletal progenitors, respectively). *Chmp5*
145 deletion in *Chmp5*^{Ctsk} periskeletal progenitors was confirmed by gene expression analysis
146 (**Fig. 2B**). Strikingly, when cultured in the osteogenic differentiation medium, *Chmp5*^{Ctsk}
147 periskeletal progenitors showed considerably enhanced osteogenesis in comparison with
148 *Chmp5*$^{Ctsk/+}$ control cells, as shown by alizarin red staining, von Kosaa staining, and
149 alkaline phosphatase activity assay (**Fig. 2C**).

150

151 The regulation of osteogenesis by CHMP5 in skeletal progenitors was further
152 determined in the osteogenic cell line MC3T3-E1 after removing *Chmp5* using
153 CRISPR/CAS9 technology (**Fig. 2D**). The deletion of *Chmp5* in MC3T3-E1 cells also
154 markedly increased osteogenesis, as shown by alizarin red staining at 2 weeks and 3

155 weeks of osteogenic induction (**Fig. 2E**). Consistently, the ingenuity pathway analysis of
156 RNA-seq data of *Chmp5*^{Ctsk} vs. *Chmp5*$^{Ctsk/+}$ periskeletal progenitors showed that multiple
157 molecular pathways related to osteoblast differentiation were activated with the *Chmp5*
158 deletion (**Fig. 2F**). Taken together, these results reveal a function of CHMP5 in regulating
159 osteogenesis in skeletal progenitors.
160

161 **CHMP5 controls skeletal progenitor cell senescence**

162 To gain more insight into the mechanism of regulation of bone formation by CHMP5, we
163 assumed that depletion of *Chmp5* in osteogenic lineage cells also increases cell
164 proliferation, which contributes to the bone overgrowth in *Chmp5* conditional knockout
165 mice. Unexpectedly, *Chmp5*^{Ctsk} periskeletal progenitors showed a significant decrease in
166 the cell proliferation rate compared to *Chmp5*$^{Ctsk/+}$ controls (approximately 58% decrease
167 in the cell number on day 6 of P2 culture, **Fig. 3A**). Because CHMP5 has been reported
168 to regulate thymocyte apoptosis [9], we performed cell apoptosis analyses for *Chmp5*^{Ctsk}
169 and *Chmp5*$^{Ctsk/+}$ cells. Annexin V staining showed that approximately 4.96 ± 0.81% of
170 *Chmp5*^{Ctsk} periskeletal progenitors vs. 1.69 ± 0.68% of *Chmp5*$^{Ctsk/+}$ control cells were
171 positively stained (**Fig. S3A**). Similarly, the in-situ terminal deoxynucleotidyl transferase
172 dUTP nick end labelling assay (TUNEL) demonstrated that around 3.70 ± 0.72% cells in
173 the periskeletal lesion of *Chmp5*^{Ctsk} mice were positively labelled (**Fig. S3B**). These
174 results show that cell apoptosis is activated in *Chmp5*^{Ctsk} periskeletal progenitors in a
175 rather low ratio.
176

177 Notably, the low apoptotic cell ratio (approximately 5%) could not well match the
178 decrease in cell proliferation rate (approximately 58%) in *Chmp5*^{Ctsk} periskeletal
179 progenitors. We further analyzed the RNA-seq data of *Chmp5*^{Ctsk} vs. *Chmp5*$^{Ctsk/+}$ cells to
180 dig out the mechanism of CHMP5 deficiency on the fate of skeletal progenitors. The gene
181 set enrichment analysis (GSEA) showed significant enrichment of genes in multiple
182 molecular pathways associated with cell senescence in *Chmp5*^{Ctsk} relative to *Chmp5*$^{Ctsk/+}$
183 periskeletal progenitors, including *Hmga1*, *Hmga2*, *Trp53*, *Ets1*, and *Txn1* (**Fig. 3B and**
184 **C**). Furthermore, Western blot results showed that both the p16 and p21 proteins, two
185 canonical markers of cellular senescence, were upregulated in *Chmp5*^{Ctsk} compared to
186 control cells, with a higher degree of upregulation in the p16 protein (**Fig. 3D**). C*hmp5*^{Ctsk}
187 mice were found to show gross accelerated aging-related phenotypes, including hair loss,
188 joint stiffness/contracture, and decreased motility (**Fig. 3E**).
189
190 To further characterize the effect of CHMP5 on skeletal progenitor cell fate, we
191 deleted *Chmp5* in ATDC5 cells, which were shown to be an appropriate model of
192 periskeletal progenitors in a previous study [23], using CRISPR/CAS9 technology (**Fig.**
193 **3F**). Similarly, *Chmp5* deletion also significantly suppressed the cell proliferation rate of
194 ATDC5 cells and mildly increased cell apoptosis (**Fig. S3C and D**). However, inhibition
195 of cell apoptosis using the pancaspase inhibitor Q-VD-Oph could not reverse cell number
196 reduction (**Fig. S3E**), indicating that cell apoptosis was not the main cause of the
197 decrease in the proliferation rate of *Chmp5*-deficient skeletal progenitors. Instead, cell
198 cycle analysis showed a significant decrease of *Chmp5*-deficient ATDC5 cells in phase
199 S, and a significant proportion of these cells were arrested in G0/G1 or G2/M phases (**Fig.**

200 **3G**), which is a typic characteristic of cell cycle arrest in senescent cells. Taken together,
201 these results at molecular, cellular, and gross levels demonstrate that *Chmp5* deficiency
202 induces skeletal progenitor cell senescence.
203

204 Secretory phenotype of *Chmp5*-deficient skeletal progenitors

205 A remarkable feature of senescent cells is the senescence associated secretory
206 phenotype (SASP), which plays a critical role in mediating the pathophysiological
207 processes of cell senescence [24]. In particular, periskeletal overgrowths in
208 *Chmp5*^{Ctsk};*Rosa26*$^{mTmG/+}$ mice showed evident integration of many cells lacking evidence
209 of Cre-mediated recombination (GFP^{-}) (**Fig. 1E**), suggesting that *Chmp5*-deleted
210 periskeletal progenitors might recruit neighboring *wild-type* cells to facilitate the bone
211 overgrowth. Additionally, the GSEA of RNA-seq data showed a significant enrichment of
212 genes associated with the SASP molecular pathway in *Chmp5*-deleted periskeletal
213 progenitors (**Fig. 4A**). Meanwhile, confocal fluorescence microscopy captured many
214 extracellular vesicles shed from the plasma membrane of *Chmp5*^{Ctsk} periskeletal
215 progenitors, which were rarely detected around *wild-type* control cells (**Fig. 4B**).
216 Furthermore, nanoparticle tracking analysis demonstrated higher concentrations of
217 extracellular vesicles in the culture medium of *Chmp5*^{Ctsk} periskeletal progenitors
218 compared to *wild-type* control cells (**Fig. 4C, D** and **Fig. S4A**). These results show that
219 *Chmp5* deficiency activates the SASP molecular pathway and increases the secretion of
220 skeletal progenitors.
221

222 Functionally, conditioned medium collected from *Chmp5*-deficient skeletal
223 progenitors caused a higher proliferation rate of ATDC5 cells than medium from control
224 cells (**Fig. 4E**). Simultaneously, $CD45^-$;$CD31^-$;GFP^- skeletal progenitors from periskeletal
225 tissues of *Chmp5*^{Ctsk};*Rosa26*$^{mTmG/+}$ mice showed increased proliferation along with
226 enhanced osteogenic differentiation compared to the corresponding cells from *Ctsk-*
227 *Cre;Rosa26*$^{mTmG/+}$ control mice (**Fig. 4F, G** and **Fig. S4B, C**). Immunostaining for the cell
228 proliferation marker Ki-67 demonstrated an increase in the number of stained cells in the
229 periskeletal lesion of *Chmp5*^{Ctsk} mice (**Fig. S4D**). Since GFP^+ *Chmp5*^{Ctsk} periskeletal
230 progenitors showed a decreased cell proliferation rate and increased cell senescence
231 (**Fig. 3**), and the GFP^- *Chmp5*^{Ctsk} periskeletal progenitors showed an increased cell
232 proliferation rate (**Fig. 4F** and **Fig. S4B**), these Ki-67^+ cells in **Fig. S4D** should represent
233 GFP^- skeletal progenitors in the periskeletal lesion. Together, these results demonstrate
234 that *Chmp5*-deficient skeletal progenitors could promote the proliferation and
235 osteogenesis of surrounding *wild-type* skeletal progenitors through the SASP.
236
237 Next, we performed a secretome analysis to characterize secretory profiles of
238 *Chmp5*^{Ctsk} vs. *wild-type* periskeletal progenitors. Fifteen proteins were found to increase
239 and five proteins to decrease in the cell supernatant of *Chmp5*^{Ctsk} periskeletal progenitors
240 (**Fig. 4H** and **Fig. S4E**). In particular, all 15 upregulated proteins, including NCAM1,
241 CSPG4, SDF4, NME2, TAGLN, OLFML2B, PXDN, COL4A1, FSTL1, TPI1, MFGE8,
242 COL1A2, COL1A1, HSPG2, and COL3A1, have been identified in the osteoblastic cell
243 secretome or in the regulation of osteoblast differentiation or functions [25, 26]. Western
244 blot verified upregulation of two of these proteins, COL1A1 and TAGLN, in the cell

245 supernatant of *Chmp5*^{Ctsk} vs. *wild-type* periskeletal progenitors (**Fig. 4I**). Together, these
246 results demonstrate the secretory phenotype and paracrine actions of *Chmp5*-deficient
247 skeletal progenitors.
248

249 Senolytic treatment mitigates musculoskeletal pathologies in *Chmp5* 250 conditional knockout mice

251 To affirm the role of cell senescence in contributing to bone overgrowth in *Chmp5*^{Ctsk} and
252 *Chmp5*^{Dmp1} mice, we treated *Chmp5*-dificient periskeletal progenitors and animals with
253 the senolytic drugs quercetin and dasatinib (Q + D), which have been widely used to
254 eliminate senescent cells under various physiological and pathological conditions [27, 28],
255 and assessed the therapeutic efficacy. First, in vitro Q + D treatment showed that
256 *Chmp5*^{Ctsk} periskeletal progenitors were more sensitive to senolytic drugs for cell
257 apoptosis compared to the control cells (**Fig. 5A**). *Chmp5*^{Ctsk} animals were then treated
258 with Q + D from the first two weeks after birth for 7 weeks and showed significantly
259 improved periskeletal bone overgrowth and animal motility compared to *Chmp5*$^{fl/fl}$ control
260 animals (**Fig. 5B** and **Fig. S5**).
261

262 Similarly, treatment of *Chmp5*^{Dmp1} mice with Q + D also improved musculoskeletal
263 manifestations, including hindlimb abduction and cortical bone thickness, and partially
264 restored skeletal muscle functions (**Fig. 5C-E**). An improvement in animal motility was
265 also found with Q + D treatment in adult mice. There were no apparent abnormalities in
266 *Chmp5*$^{fl/fl}$ control animals treated with the same dose of Q + D in parallel. Together, these
267 results demonstrate that the elimination of senescent cells using senolytic drugs is

268 effective in alleviating musculoskeletal pathologies in *Chmp5*^{Ctsk} and *Chmp5*^{Dmp1} animals,
269 confirming that cell senescence is responsible for musculoskeletal abnormalities in
270 *Chmp5*^{Ctsk} and *Chmp5*^{Dmp1} mice.
271

272 CHMP5 is essential for endolysosomal functions and maintaining 273 VPS4A protein in skeletal progenitors

274 Next, we wondered whether *Chmp5* deficiency in skeletal progenitors affects the
275 endocytic pathway. Notably, approximately 45% of *Chmp5*^{Ctsk} periskeletal progenitors
276 contained enlarged GFP^{+} vesicles, which were rarely found in *wild-type Ctsk*$^{+}$ periskeletal
277 progenitors (**Fig. 6A**), suggesting a possible issue of the endocytic pathway in *Chmp5*-
278 deleted skeletal progenitors. Next, we used molecular markers for different components
279 and the function of the endocytic pathway to elucidate the influence of *Chmp5* deficiency
280 on the endolysosomal system in skeletal progenitors (**Fig. 6B**).
281

282 The LysoTracker Red DND-99 trace and the immunostaining of lysosome-
283 associated membrane protein 1 (LAMP1) showed positive staining in many of the
284 enlarged vesicles in *Chmp5*^{Ctsk} periskeletal progenitors (**Fig. 6C** and **Fig. S6A, B**). The
285 quantification of the number and average size of LAMP1 stained vesicles were further
286 performed in ATDC5 cells with or without *Chmp5* deletion (**Fig. 6D**). Next, the number
287 and size of the vesicles stained for the late endosome marker RAB7 also increased
288 markedly in *Chmp5*-deficient relative to *wild-type* skeletal progenitors (**Fig. 6E, F**).
289 Meanwhile, many of these accumulated vesicles were double positive for LAMP1 and
290 RAB7 (**Fig. S6C, D**), suggesting that they are terminal compartments in the endocytic

291 pathway. Accordingly, the transmission electron microscopy demonstrated a significant
292 accumulation of MVB-like and lysosome-like structures with different electronic density in
293 *Chmp5*^{Ctsk} periskeletal progenitors (**Fig. 6G**).
294
295 To examine the function of the endocytic pathway, we used a pH-sensitive
296 fluorescent EGF conjugate and traced the degradation of the internalized EGF receptor
297 in *Chmp5*^{Ctsk} vs. *wild-type* periskeletal progenitors. *Chmp5* deficiency significantly
298 delayed the degradation of the EGF conjugate in *Chmp5*^{Ctsk} periskeletal progenitors (**Fig.**
299 **6H**), indicating altered function of the endocytic pathway. It should be noted that the early
300 endosomes of EEA1^{+} also increased slightly in approximately 10% of *Chmp5*^{Ctsk}
301 periskeletal progenitors, while the recycling endosomes of RAB11^{+} and the TGN38^{+} trans-
302 Golgi network were relatively normal (**Fig. S6E**). These results demonstrate that CHMP5
303 deficiency in skeletal progenitors causes the accumulation of late endosomes and
304 lysosomes and disrupts the function of the endolysosomal pathway.
305
306 To dissect the molecular mechanism of CHMP5 that regulates the endolysosomal
307 pathway, we performed a proteomic analysis in *Chmp5*^{Ctsk} and *wild-type* periskeletal
308 progenitors. Bioinformatic analyses of proteomic data showed that VPS4A is one of the
309 most significant decreased proteins in *Chmp5*^{Ctsk} compared to *wild-type* periskeletal
310 progenitors (**Fig. 6I**). The decrease in the VPS4A protein in *Chmp5*^{Ctsk} periskeletal
311 progenitors was verified by Western blot analysis (**Fig. 6J**), while the *Vps4a* mRNA did
312 not show a significant change in the RNA-seq analysis (**Fig. S6F**). On the other hand,
313 when CHMP5 was overexpressed by transfection of a CHMP5 vector into HEK-293T cells,

314 the level of VPS4A protein increased significantly and *VPS4A* mRNA was not significantly
315 affected (**Fig. S6G, H**). These results indicate that CHMP5 is essential in maintaining the
316 VPS4A protein. Since VPS4A is a critical ATPase mediating the function of the ESCRT-
317 III protein complex, the reduction of VPS4A protein could be responsible for
318 endolysosomal dysfunction in *Chmp5*-deleted skeletal progenitors.
319

320 Mitochondrial dysfunction is responsible for cell senescence in 321 *Chmp5*-deleted skeletal progenitors

322 A remaining question is how *Chmp5* deficiency and endolysosomal dysfunction cause
323 skeletal cell senescence. Impairment of lysosomal functions could hinder the degradation
324 of damaged mitochondria, resulting in the accumulation of reactive oxygen species (ROS)
325 in mitochondria [29, 30]. Indeed, the GSEA of RNA-seq data showed significant
326 enrichment of genes associated with the molecular pathway of oxidative stress-induced
327 cell senescence in *Chmp5*^{Ctsk} vs. *Chmp5*$^{Ctsk/+}$ periskeletal progenitors (**Fig. 7A**).
328 Accordingly, the level of mitochondrial ROS and the abundance of mitochondria
329 increased markedly in *Chmp5*-deficient compared to *wild-type* skeletal progenitors, as
330 shown by CellRox, tetramethylrhodamine methyl ester (TMRE), and MitoTracker
331 fluorescence stain, and expression levels of mitochondrial inner membrane proteins
332 NDUF88, SDHB, and ATP5A (**Fig. 7B to D** and **Fig. S7A, B**).
333

334 Mitochondrial functions were also compromised in *Chmp5*-deficient skeletal
335 progenitors as shown by decreased mitochondrial respiratory capacity, increased
336 extracellular acidification rate, and reduced tolerance to galactose (**Fig. 7E and F**).

337 Furthermore, mitochondrial dysfunction and DNA damage response usually form a
338 feedback loop to drive senescent cell phenotypes [31-33]. The GSEA of the RNA-seq
339 data also showed enrichment of genes associated with DNA damage-induced cell
340 senescence in *Chmp5*^{Ctsk} vs. *Chmp5*$^{Ctsk/+}$ skeletal progenitors (**Fig. S7C**). Upregulation
341 of two critical DNA damage-responsive genes *H2afx* and *Trp53* was verified by qPCR in
342 *Chmp5*^{Ctsk} relative to *Chmp5*$^{Ctsk/+}$ skeletal progenitors (**Fig. S7D**). Importantly, N-
343 Acetylcysteine (NAC) antioxidant treatment could reverse the reduced activity of cell
344 proliferation in *Chmp5*-deficient skeletal progenitors (**Fig. 7G**). Therefore, the
345 accumulation of dysfunctional mitochondria and mitochondrial ROS is responsible for cell
346 senescence in *Chmp5*-deficient skeletal progenitors.

347 ## Discussion

348 In this study, our results reveal the role and mechanism of CHMP5 in the regulation of
349 cell senescence and bone formation in osteogenic cells. In normal skeletal progenitor
350 cells, CHMP5 is essential in maintaining the VPS4A protein, a critical AAA ATPase for
351 the functions of the ESCRT-III protein complex. The deficiency of CHMP5 decreases the
352 VSP4A protein and causes the accumulation of dysfunctional late endosomes (MVB),
353 lysosomes, and mitochondria, which induce skeletal cell senescence and result in
354 increased bone formation through a combination of cell-autonomous and paracrine
355 mechanisms (**Fig. 7H**). Strikingly, elimination of senescent cells using senolytic drugs is
356 effective in mitigating abnormal bone formation.

357

358 The role of CHMP5 in cell senescence has not been reported. As the mechanisms
359 and functions of cell senescence could be highly heterogeneous depending on inducers,
360 tissue and cell contexts, and other factors such as “time” [34-36], there is currently no
361 universal molecular marker to define all types of cell senescence. In this study, *Chmp5*-
362 deficient skeletal progenitors show multiple canonical features of senescent cells,
363 including increased p16 and p21 proteins, cell cycle arrest, elevated secretory phenotype,
364 accumulation and dysfunction of lysosomes and mitochondria. Also, *Chmp5*^{Ctsk} and
365 *Chmp5*^{Dmp1} mice show dramatic aging-related phenotypes, including hair loss, joint
366 stiffness/contracture, decreased bone strength, or gradual loss of muscle mass and
367 functions. Importantly, senolytic drugs (Q + D) markedly improve musculoskeletal
368 abnormalities and increase animal motility in *Chmp5*^{Ctsk} and *Chmp5*^{Dmp1} mice. These
369 results reveal the role of CHMP5 in controlling the senescence of skeletal cells.

370

371 CHMP5 has been reported to regulate VPS4 activity, which catalyzes the
372 disassembly of the ESCRT-III protein complex from late endosomes/MVBs, by binding
373 directly to the VPS4 protein or other protein partners such as LIP5 and Brox [37, 38].
374 However, it remains unknown how CHMP5 regulates VPS4 activity. Our results in this
375 study show that CHMP5 is necessary to maintain the VPS4A protein but does not affect
376 the level of VPS4A mRNA, suggesting that CHMP5 regulates VPS4 activity by
377 maintaining the level of the VPS4A protein. However, the mechanism of CHMP5 in the
378 regulation of the VPS4A protein has not yet been studied. Since CHMP5 can recruit the
379 deubiquitinating enzyme USP15 to stabilize IκBα in osteoclasts by suppressing
380 ubiquitination-mediated proteasomal degradation [8], it is also possible that CHMP5
381 stabilizes the VPS4A protein by recruiting deubiquitinating enzymes and regulating
382 ubiquitination-mediated proteasomal degradation of VPS4A, which needs to be clarified
383 in future studies. Notably, mutations in the *VPS4A* gene in humans can cause
384 multisystemic diseases, including musculoskeletal abnormalities [39] (OMIM: 619273),
385 suggesting that normal expression and function of VPS4A are important for
386 musculoskeletal physiology.

387

388 The upstream signaling that regulates CHMP5 expression in osteogenic cells is
389 unclear. Previous studies showed that muramyl-dipeptide and lipopolysaccharide
390 upregulate CHMP5 expression in human monocytes [40, 41]. Whether the mechanism
391 also occurs in osteogenic cells remains to be determined, especially since many
392 molecular and cellular mechanisms are cell lineage/type dependent. In addition, an earlier

393 study showed that *Rank* haploinsufficiency in *Chmp5*^{Ctsk} mice (*Chmp5*^{Ctsk}*;Rank*$^{+/-}$) could
394 greatly reverse skeletal abnormalities in these animals, including periskeletal overgrowth
395 [8]. Therefore, RANK receptor signaling may function upstream of CHMP5. However,
396 whether RANK is expressed in osteogenic cells needs additional studies to clarify.
397 Otherwise, other epigenetic, transcriptional, translational, or post-translational
398 mechanisms may also play a role in the regulation of CHMP5 expression in osteogenic
399 lineage cells in physiological and pathological contexts.
400
401 A previous study using the *Chmp5*^{Ctsk} mouse model defined a function of CHMP5
402 in the regulation of osteoclast differentiation by tuning NF-κB signaling [8]. While the
403 evidence on the role of CHMP5 in osteoclastogenesis is robust in that study, our results
404 in the current study provide compelling evidence on the role of CHMP5 in bone formation
405 in osteogenic cells. Additionally, the function of CHMP5 in restricting bone formation was
406 confirmed in the *Chmp5*^{Dmp1} mouse model and in the MC3T3-E1 cell model (Figs. 1 and
407 2). Therefore, it is probable that both osteoblasts and osteoclasts contribute to bone
408 deformation in *Chmp5*^{Ctsk} mice. However, the previous study by Greenblatt et al. did not
409 find any endolysosomal abnormalities in osteoclasts and in that study cell senescence
410 and mitochondrial functions were not measured. Therefore, our results in this study
411 predominantly reveal a novel function and related mechanism of CHMP5 in the regulation
412 of bone formation in osteogenic cells. Intriguingly, bone overgrowth was confined to the
413 periosteal or endosteal site in *Chmp5*^{Ctsk} and *Chmp5*^{Dmp1} mice, respectively, pointing to
414 a site-specific function of CHMP5 or cell senescence in regulating bone formation.
415

416 In addition, there was also a mild increase in apoptotic cells in the population of
417 *Chmp5*-deficient skeletal progenitors (approximately 5%). Since anti-apoptotic treatment
418 with the pan-caspase inhibitor Q-VD-Oph could not reverse the decrease in cell number
419 in *Chmp5*-deficient skeletal progenitors, cell apoptosis may not be the main cause of the
420 decrease in cell proliferation rate in these progenitors. It should be noted that although
421 senescent cells are generally resistant to apoptosis, the gradual accumulation of
422 dysfunctional lysosomes and mitochondria in *Chmp5*-deficient skeletal progenitors could
423 result in overload of toxic macromolecules and metabolites, which could activate the
424 apoptotic pathway to eliminate severely damaged cells. Otherwise, CHMP5 may regulate
425 cell senescence and apoptosis through different mechanisms.
426
427 In summary, we have revealed the role of CHMP5 in the regulation of cell
428 senescence and bone formation in osteogenic cells. This study also confirms the
429 essential function of CHMP5 in the endolysosomal pathway that involves the regulation
430 of the VPS4A protein. Additionally, mitochondrial functions are impaired with CHMP5
431 deletion, which is responsible for cell senescence. Future studies should explore the
432 mechanism of CHMP5 in the regulation of mitochondrial functions. Since $Chmp5^{Ctsk}$ and
433 $Chmp5^{Dmp1}$ mice recapitulate many cellular and phenotypic features of musculoskeletal
434 lesions in lysosomal storage disease, these animals could be used as preclinical models
435 to investigate the mechanism and test therapeutic drugs for these intractable disorders.
436

Acknowledgments

We thank Dr. Sankar Ghosh for providing *Chmp5*-floxed mice; Drs. Gregory Hendricks and Lara Strittmatter at the University of Massachusetts Chan Medical School for help in interpreting TEM data; Dr. Tomer Shpilka for assistance in running the Seahorse analyzer; Drs. Guangchuang Yu and Jiyeon Park for independently analyzing the RNA-seq data. Dr. Chunjing Bian for generating the CHMP5 overexpression vector. X.G. is supported by the National Natural Science Foundation of China (project 2-2-008-0213) and the Beijing Natural Science Foundation (project 5222008). J.H.S. holds support from the NIH (R21AR077557, R01AR078230) and AAVAA Therapeutics.

Contributions

X.G. perceived the project, designed experiments, interpreted the results, and wrote and reviewed the manuscript; F.Z., Y.W., L.Z., C.W. and X.G. performed experiments and analyzed the results; D.C. and R.X. provided critical resources for the study; H.L. contributed to part of RNA-seq data analyses; C.M.H. offered suggestions and main reagents for mitochondrial analyses; J.H.S. partly supported the study and reviewed the manuscript.

Competing interests

The study started when the corresponding author (X. Ge) worked at the University of Massachusetts Medical School and a previous manuscript related to this study was posted on bioRxiv (https://doi.org/10.1101/2020.08.03.233874). To complete the study for a peer-reviewed publication, the co-first authors and X. Ge generated a novel *Chmp5*-

460 floxed mouse strain, re-established all animal and cell models in the current laboratory in
461 Beijing, China, and added novel critical experiments to make the conclusion convincing
462 and the study comprehensive. Therefore, we reorganized the data and wrote it as a new
463 paper. All authors agree on the current version of the paper, including its authorship and
464 conclusions. J.H.S. is a scientific co-founder of AAVAA Therapeutics and holds equity in
465 this company but does not have conflicts of interest with this study. Other authors declare
466 no competing interests.

467 # Methods

468 ## Mice

469 In this study, two *Chmp5*-flox mouse strains were used, and similar phenotypes were
470 observed. The *Chmp5*$^{tm2.1Gho}$ strain was previously described [8]. The alternative *Chmp5*-
471 flox strain was established by CRISPR/Cas9-mediated genome engineering. Similarly to
472 the *Chmp5*$^{tm2.1Gho}$ strain, exons 4 and 5 were selected as the conditional knockout region
473 in the newly created strain and deletion of this region results in frameshift of the *Chmp5*
474 gene. To engineer the target vector, homologous arms, and the conditional knockout
475 region with 5' and 3' loxP sites were generated by PCR using the BAC clone. Cas9, gRNA,
476 and targeting vectors were co-injected into fertilized eggs for gene-edited mouse
477 production and pups were genotyped by PCR followed by sequencing analysis. Mice
478 bearing the targeted allele were backcrossed with C57BL/6J mice up to F8 generation.

479

480 Ctsk$^{tm1(cre)Ska}$ (Ctsk^{Cre}), B6N.FVB-Tg(Dmp1-cre)1Jqfe/BwdJ (Dmp1-Cre), B6.Cg-
481 Tg(Prrx1-cre)1Cjt/J (Prrx1^{Cre}), B6;SJL-Tg(Col2a1-cre)1Bhr/J (Col2-Cre), and B6.Cg-
482 Tg(Sp7-tTA,tetO-EGFP/cre)1Amc/J (Osx1-GFP::Cre) mice have previously been
483 reported [8, 17, 42-44]. While the Ctsk-Cre strain is a knockin mouse line, other strains
484 (Dmp1-Cre, Prrx1-Cre, Col2-Cre, and Osx-Cre) are transgenic lines. The
485 Gt(ROSA)26Sor$^{tm4(ACTB-tdTomato,-EGFP)Luo}$ (Rosa26^{mTmG}) mice were purchased from Jackson
486 Laboratories. To generate experimental animals, *Chmp5*$^{fl/fl}$ mice were crossed with
487 *Chmp5*$^{Ctks/+}$ and *Chmp5*$^{Dmp1/+}$ mice, respectively. To generate reporter mouse lines,
488 *Chmp5*$^{Ctks/+}$ mice were mated with *Chmp5*$^{fl/fl}$;*Rosa26*^{mTmG} mice, and Ctsk^{Cre} mice were
489 crossed with Rosa26^{mTmG} animals.

490

491 All mice were kept in C57BL/6J background and housed in the standard animal
492 facility on a 12-hour light/dark cycle with ad libitum access to water and standard chow.
493 In most situations, the littermates were compared otherwise as indicated. All animals
494 were used in accordance with the Guide for Care and Use of Laboratory Animals (NIH,
495 United States) and were handled according to protocols approved by IACUC at the
496 University of Massachusetts Medical School (Worcester, United States) and Capital
497 Medical University (Beijing, China). The biological and technical replicates (*n* numbers)
498 for each animal experiment are reported in the figure legends. In this study, both sexes
499 of mice were used and, unless otherwise stated, no gender differences were observed in
500 the reported phenotypes.

501

502 **Micro-CT and radiography**

503 Micro-CT analyses were performed using the Scanco μCT-35 or μCT-40 scanner
504 (Scanco Medical). Images were processed using the Inveon Research Workplace
505 (Siemens Medical Solutions). X-ray images were acquired using the X-Ray MX-20
506 Specimen (Faxitron) following the default programme.

507

508 **Histology, immunohistochemistry, and immunofluorescence**

509 All samples were fixed in 10% neutral formalin or 4% paraformaldehyde overnight for
510 premature samples or 2 days for mature skeletal samples. Samples were decalcified
511 with 14% EDTA and serial sections were cut for all samples. At least five slides were
512 selected at a certain interval (80-100 μm) from each sample for histological evaluation.

513 Fate-mapping images were acquired using a Leica TCS SP5 II laser scanning confocal
514 microscope.
515
516 Immunohistochemistry for Ki-67 was performed using the VECTASTAIN® Elite®
517 ABC HRP Kit (Peroxidase, Rabbit IgG; Vector Laboratories). Cells for
518 immunofluorescence were cultured in 35 mm MatTek glass bottom dishes (No. 1.5
519 coverslip, MatTek Corporation). Briefly, cells were fixed in 4% PFA for 15 min, blocked
520 in 1% BSA for 30 min, and incubated with primary antibodies for 2 hrs and then
521 fluorescence conjugated secondary antibodies for 1 hr. Images were acquired using
522 the Leica TCS SP5 II laser scanning confocal microscope. The quantification of
523 intracellular vesicles was performed using FIJI software following the particle analysis
524 procedure (https://imagej.net/imagej-wiki-static/Particle_Analysis, NIH).
525
526 **Bone mechanical test**
527 The femurs of *Chmp5*^{Ctsk} and *Chmp5*$^{fl/fl}$ mice at 6-7 weeks of age were subjected to
528 mechanical testing using the DMA Q800 mechanical test system with the 3-point
529 bending mode following the manufacturer's procedure (TA Instruments, USA). The
530 femurs were placed in a direction of the anterior surface downward and the posterior
531 aspect of the femoral condyles facing upward. The span length (L) was 10 mm and the
532 load was applied in the middle of the bone. Five mice per group were used and bone
533 stiffness and ultimate stress (fracture stress) from male mice were reported. Similar
534 changes were observed in both sexes.
535

536 **Tests of skeletal muscle functions**

537 The four-limb hanging test was performed using the top grid of a mouse cage [45]. The
538 grid was set at a height of about 35 cm, and the measurement was repeated for 3-5
539 times for each mouse at a rest interval of about 3-5 min. The maximum hang time was
540 recorded for each animal. Both male and female animals were included in this
541 experiment, and there was no significant sex difference regarding the four-limb hanging
542 time.

543

544 The forelimb grip strength test was carried out using an electronic scale as
545 described with slight modification [45, 46]. A mouse was allowed to grasp the gauze
546 attached on the scale. The scale was reset to 0 g after stabilization and a researcher
547 slowly pulled the mouse's tail backward. Five consecutive measurements were
548 performed for each mouse and the peak pull force in grams was recorded. A significant
549 sex difference was observed in the forelimb grip strength. Both male and female mice
550 were included in this study and the same trend of changes was found in both genders.

551

552 **Skeletal progenitor cell culture and sorting**

553 The periskeletal progenitors were isolated from the hindlimbs of *Ctsk-*
554 *Cre;Rosa26*$^{mTmG/+}$, *Chmp5*$^{Ctsk/+}$*;Rosa26*$^{mTmG/+}$, and *Chmp5*^{Ctsk}*;Rosa26*$^{mTmG/+}$ mice (*n* =
555 10 animals per genotype) at 2 weeks of age according to the previously established
556 method [23]. Briefly, the periskeletal tissues were dissected, minced into small pieces,
557 and digested with 1 mg/ml collagenase type I (Worthington), 1 mg/ml collagenase type
558 II (Worthington) and 1.5 mg/ml dispase (Roche) for 30 min at 37°C. Cells were cultured

559 in skeletal stem cell medium (Joint Therapeutics, Beijing, China) for one week, stained
560 with anti-CD31 and anti-CD45 antibodies, and sorted using a FACSAria II cell sorter
561 (BD Biosciences) for further analyses. In all experiments, *Chmp5*^{Ctsk} and control cells
562 from littermate mice were cultured, sorted, and re-seeded in parallel for subsequent
563 analyses. The biological and technical replicates (*n*-numbers) for each cellular
564 experiment are reported in the figure legends.
565
566 **CRISPR/CAS9 lentiviral infection**
567 Pairs of CRISPR guide RNA oligos (mouse *Chmp5* single guide RNAs [sgRNAs] targeting
568 GGCTCCGCCACCTAGCTTGA and GTTTCGCTTTTCCGAAGAAT on exon 1
569 respectively) were annealed and cloned into the BsmBI sites of the lentiCRISPR V2-puro
570 vector (plasmid 52961, Addgene). CRISPR lentiviral plasmids and lentiviral packaging
571 plasmids (pMDLg/pRRE, pRSV-Rev, and pMD2.G; Addgene) were transfected into HEK
572 293T cells. The supernatants were harvested and filtered through a 0.45-μm filter 2.5
573 days after transfection. MC3T3-E1 and ATDC5 cells were infected with CRISPR lentivirus
574 and selected with puromycin (4.5 μg/ml, Clontech) for 7 days. The depletion of *Chmp5*
575 was confirmed by Western blotting.
576
577 ***In vitro* osteogenesis**
578 For osteogenic differentiation, 1.0 x 10^5 cells were seeded in each well of 24-well plates
579 and cultured overnight. Cells were changed into osteogenic media (Joint Therapeutics)
580 the next day and induced for the indicated times. Osteogenesis was determined by

581 alizarin red and von Kossa staining and by examining the activity of alkaline
582 phosphatase.
583
584 **Cell cycle, proliferation, and apoptosis analyses**.
585 The cell number was counted with a Countess II FL Automated Cell Counter
586 (ThermoFisher Scientific, USA) at indicated time intervals. The AlamarBlue cell viability
587 assay was performed as previously described [23]. The cell cycle was determined using
588 the APC-BrdU Flow Kit (BD Biosciences). In vitro apoptosis analysis was carried out
589 with Annexin V-PI staining and in situ cell apoptosis was determined with TUNEL
590 staining (Abcam).
591
592 **RNA-seq, data analysis, and functional annotation**
593 The sorted *Chmp5*^{Ctsk} and *Chmp5*$^{Ctsk/+}$ periskeletal progenitors were subjected to RNA-
594 seq For library preparation, 100 ng of total RNA from each sample was subjected to rRNA
595 depletion with the NEBNext rRNA Depletion Kit (New England Biolabs) according to the
596 manufacturer's manual. Subsequently, the rRNA-depleted RNA was used to build the
597 RNA-seq library with the NEBNext Ultra II Directional RNA Library Prep Kit (New England
598 Biolabs) according to the manufacturer's manual. The index of each RNA-seq library was
599 introduced using NEBNext Multiplex Oligos for Illumina (New England Biolabs). Each
600 RNA-seq library was analyzed by the fragment analyzer (Advanced Analytical
601 Technologies) and quantified by the KAPA Library Quantification Kit (KAPA Biosystems)
602 according to the manufacturer's manual. An equal amount of each RNA-seq library was

603 mixed for sequencing in one lane of Illumnia HiSeq3000 in paired-end 150 base mode
604 (Illumina).
605
606 The raw Illumina pair-end reads were first aligned with ribosomal RNA (GenBank ID
607 BK000964.1) with Bowtie2 v2.2.6 [47]. Reads that failed to map to ribosomal RNA were
608 aligned with the mouse reference genome mm10 with STAR v2.5.3 [48]. Differential
609 analysis was performed with Cuffdiff v2.2.1 [49]. The raw data were analyzed by two
610 independent statisticians and similar results were obtained.
611
612 Pathway analyses were performed for differentially expressed genes using the
613 Reactome online analysis tool [50] and the Ingenuity Pathway Analysis software (Qiagen).
614 Gene ontology term over-representation analysis was run using PANTHER (version 14.1)
615 with all genes expressed in a tissue or cell type as background and the differentially
616 expressed gene list as input. The P-values of Fisher's exact tests were corrected by
617 controlling the false discovery rate (FDR). Gene set enrichment analyses were performed
618 using GSEA or ConsensusPathDB. For GSEA-based analysis, gene sets of interests
619 were downloaded from the MsigDB, while all built-in gene sets were used for
620 ConsensusPathDB-based analysis.
621
622 **Nano LC-MS/MS for secretomic and proteomic analyses**
623 Label-free relative protein quantification analyses were performed to identify differentially
624 expressed proteins in the supernatant or cell lysis of *Chmp5*^{Ctsk} versus control periskeletal
625 progenitors (*n* =3 animals per group). For cell supernatants, the same amounts of

626 samples went through 3 kD ultrafiltration tubes and then were processed for reduction
627 and alkylation. Subsequently, the samples were digested in trypsin overnight and the
628 peptides were desalted prior to mass spectrometry analysis. For cell lysis, samples were
629 precipitated using acetone after reduction and alkylation. The samples were then
630 subjected to digestion, desalination, and mass spectrometry analysis.
631
632 Quantitative data were collected on an Orbitrap Eclipse™ Tribrid™ mass spectrometer
633 (ThermoFisher Scientific) coupled to a nanoLC system (EASY-nLC™ 1200,
634 ThermoFisher Scientific). All peptide mixtures were analyzed using the same
635 chromatographic conditions: 5 µl of each sample were fractionated in a 150 µm×15 cm
636 in-house made column packed with Acclaim PepMap RPLC C18 (1.9 µm, 100 Å, Dr.
637 Maisch GmbH, Germany) working at a flow rate of 600 nl/min, using a linear gradient of
638 eluent B (20% 0.1% formic acid in water + 80% acetonitrile) in A (0.1% formic acid in
639 MilliQ water) from 4% to 10% for 5 min, 10% to 22% for 80 min, 22% to 40% for 25 min,
640 40% to 95% for 5 min, and 95% to 95% for 5 min. MS/MS analyses were performed using
641 Data-Dependent Acquisition (DDA) mode: one MS scan (mass range from 350 to 1500
642 m/z) was followed by MS/MS scans up to the top 20 most intense peptide ions from the
643 preview scan in the Orbitrap, applying a dynamic exclusion window of 120 seconds.
644
645 The raw MS files were analyzed and searched against the Mus_musculus_reviewed
646 protein database using MaxQuant (1.6.2.10). The parameters were set as follows: the
647 protein modifications were carbamidomethylation (C) (fixed), oxidation (M) (variable),
648 acetyl (Protein N-term) (variable); the enzyme specificity was set to trypsin; the maximum

649 missed cleavages were set at 2; the precursor ion mass tolerance was set at 20 ppm;
650 and the MS/MS tolerance was 20 ppm. Only highly confident identified peptides were
651 chosen for downstream protein identification analysis.
652
653 **Western blotting**
654 Western blot was performed using 4–20% Mini-PROTEAN® TGX™ precast protein
655 gels (Bio-Rad). The following antibodies: anti-CHMP5 polyclonal antibody [6], anti-
656 COL1A1 monoclonal antibody (clone E8F4L, Cell Signaling Technology, CST), anti-
657 TAGLN polyclonal antibody (cat#: AB14106, Abcam), anti-p16 INK4A monoclonal
658 antibody (clone E5F3Y, CST), anti-p21 Waf1/Cip1 monoclonal antibody (clone E2R7A,
659 CST), anti-VPS4A monoclonal antibody (clone A-11, Santa Cruz Technology), total
660 OXPHOS antibody cocktail (Abcam), anti-GAPDH monoclonal antibody (clone 14C10,
661 CST), and anti-β-Actin monoclonal antibody (clone D6A8, CST), were used.
662
663 **Quantitative PCR**
664 Total RNA was isolated from cells using Trizol reagent (Qiagen). RNA samples were
665 treated with the TURBO DNA-free™ Kit (Thermo Fisher) and equal amounts (1–2 μg)
666 were used for reverse transcriptase reaction using an iScript™ Reverse Transcription
667 Supermix (Bio-Rad). Quantitative PCR was run using the SYBR® Green Master Mix
668 on a CFX Connect™ Real-Time PCR Detection System (Bio-Rad). Gene expression
669 levels were analyzed relative to the housekeeping gene *Gapdh* and presented by $2^{-\Delta Ct}$
670 [51]. The primer sequences were used for qPCR are as following: *Chmp5,* forward, 5'-
671 ATGAGAGAGGGTCCTGCTAAG-3', reverse, 5'-CCGTGGTCTTGGTGTCCTTTA-3';

672 *H2afx*, forward, 5'-GTGGTCTCTCAGCGTTGTTC-3', reverse, 5'-CGGCC
673 TACAGGGAACTGAA-3'; *Tp53* , forward, 5'-GTCACAGCACATGACGGAGG-3', reverse,
674 5'-TCTTCCAGATGCTCGGGATAC-3'; *Gapdh*, forward 5′-TGCCAGCCTCGTCCCG
675 TAGAC-3′, reverse 5′-CCTCACCCCATTTGATGTTAG-3′; *VPS4A*, forward 5′-
676 AGAACCAGAGTGAGGGCAAGGG-3′, reverse 5′- GCACCCATCAGCTGTTCTTGCA-3′;
677 *CHMP5*, forward 5′-CCAGCCTGACTGACTGCATTGG-3′, reverse 5′-
678 TCGCAAGGCTTTCTGCTTGACC-3′; *GAPDH*, forward 5′-
679 GGAGTCCACTGGCGTCTTCAC-3′, reverse 5′-GAGGCATTGCTGATGATCTTGAGG-3′.
680

681 **Extracellular vesicle tracking**

682 The concentration and size distribution of extracellular vesicles were analyzed using
683 the NanoSight NS300 following the manufacturer's protocol (Malvern
684 Instruments). Briefly, cells were seeded in 24-well plates at the density of 1 x 10^5 cells
685 per well and cultured overnight. The next morning, cells were changed to serum-free
686 medium and incubated for 9 hrs. The medium was collected and subjected to
687 sequential centrifugation at 300 g for 10 min, 2000 g for 20 min, and 10000 g for 30
688 min. The resulting supernatant was manually injected into the instrument and run in the
689 "standard measurement" module with five captures per sample and the data were
690 processed with a detection threshold of 2.
691

692 **Live-cell imaging for cell endocytosis**

693 The *wild-type* and *Chmp5*^{Ctsk} periskeletal progenitors were incubated on ice for 10 min
694 before adding fresh medium with 2 ug/ml pHrodo™ red EGF conjugate (ThermoFisher).

695 Cells were incubated at 37 °C for 30 min and subsequently washed and changed to
696 fresh medium. Live-cell images were obtained at 1, 12, and 24 hrs using the Leica TCS
697 SP5 II laser scanning confocal microscope.
698
699 **Transmission electron microscopy**
700 *Wild-type* and *Chmp5*^{Ctsk} periskeletal progenitors were fixed in culture plates overnight
701 at 4 °C using 2.5% glutaraldehyde in 0.1 M Na cacodylate-HCl buffer (pH 7.2). After
702 washing in 0.5 M Na cacodylate-HCl buffer (pH 7.0), the cells were post-fixed for 1 hr in
703 1% osmium tetroxide (w/v) at room temperature. After post-fixation, the culture plate with
704 adherent cells were enblock stained (20 min) with 1% aqueous uranyl-acetate (w/v).
705 Culture plates were washed again in the same buffer and dehydrated through a series of
706 graded ethanol to 100% and transferred through two changes of 50/50 (v/v) SPIpon resin
707 (Structure Probe, Inc.)/100% ethanol and left overnight to infiltrate. The following morning,
708 the cell culture plates were transferred through three changes of fresh SPIpon resin to
709 finish the infiltration and embedding and finally, the plates were filled with freshly prepared
710 SPIpon resin and polymerized for 48 hrs at 70 °C.
711
712 Once fully polymerized, the plate was cut apart, and each well was plunged into liquid
713 nitrogen to separate the SPIpon epoxy block with the embedded cells from the culture
714 dish. The round epoxy disks with the embedded cells were then examined under an
715 upright light microscope, and areas of cells were cut from the disks and glued onto blank
716 microtome studs and trimmed for ultramicrotomy. Ultrathin sections (70 nm) were cut on
717 a Reichart-Jung ultramicrotome using a diamond knife. The sections were collected and

718 mounted on copper support grids and contrasted with lead citrate and uranyl acetate and
719 examined on a FEI Tecnai G2 Spirit transmission electron microscope at 100 Kv
720 accelerating voltage and images were recorded at various magnifications using a Gatan
721 2K digital camera system.
722
723 **Mitochondrial respiration**
724 Mitochondrial respiration was examined in *Chmp5*^{Ctsk} and *wild-type* periskeletal
725 progenitors using a Seahorse XF^{e}96 Extracellular Flux Analyzer (Agilent) as previously
726 described [52]. Briefly, 10000 cells per well were seeded in XF 96-well culture plates and
727 cultured overnight. The next day, cells were changed to assay medium and incubated at
728 37 °C w/o CO2 for 1 hr. The assay was carried out using the Seahorse XF Cell Mito
729 Stress Test kit with sequential injections of Oligomycin (1 μM), FCCP (1 μM), and
730 Rotenone plus Antimycin A (0.5 μM) following the manufacturer's protocol.
731
732 **Senolytic treatments**
733 For in vitro cell treatment, *Chmp5*^{Ctsk} and control cells were seeded in 96-well plates at a
734 density of 6000 cells/ well and cultured overnight. Quercetin and dasatinib were added to
735 the culture medium at a final concentration of 50 μM and 500 nM, respectively. Apoptotic
736 cells are labeled using Incucyte Annexin V Red Dye and are quantified in real time using
737 the Incucyte Live-Cell Analysis System. Six replicates were used for each group and the
738 experiment was repeated twice using cells from two different animals per group.
739

740 For in vivo treatment, the senolytic drugs quercetin and dasatinib were administered
741 intraperitoneally weekly at 50 μg/g and 5 μg/g body weight, respectively. Senolytic
742 treatment in *Chmp5*^{Ctsk} and littermate control mice started from the first week after birth
743 and mice were collected at 7-8 weeks of age for skeletal analyses. For the *Chmp5*^{Dmp1}
744 strain, treatment began the second week after birth and the animals were monitored for
745 16 weeks.
746
747 **Statistics**
748 All data are represented as mean ± s.d.. Normality and equal variance of the data sets
749 were tested using the Shapiro-Wilk test and the F test, respectively. The data were
750 determined to be normally distributed and have equal variance unless otherwise specified.
751 For experiments with three or more groups, statistical analysis was performed using one-
752 way or two-way ANOVA followed by multiple comparisons. For comparisons between two
753 groups, the two-tailed unpaired Student's *t*-test was applied. All analyses were performed
754 with Prism 10.1.1 (GraphPad).

755 ## References

756 1. Kaksonen M, Roux A. Mechanisms of clathrin-mediated endocytosis. Nat Rev Mol Cell
757 Biol. 2018;19(5):313-26. doi: 10.1038/nrm.2017.132. PubMed PMID: 29410531.

758 2. Christ L, Raiborg C, Wenzel EM, Campsteijn C, Stenmark H. Cellular Functions and
759 Molecular Mechanisms of the ESCRT Membrane-Scission Machinery. Trends Biochem Sci.
760 2017;42(1):42-56. doi: 10.1016/j.tibs.2016.08.016. PubMed PMID: 27669649.

761 3. Luzio JP, Pryor PR, Bright NA. Lysosomes: fusion and function. Nat Rev Mol Cell Biol.
762 2007;8(8):622-32. doi: 10.1038/nrm2217. PubMed PMID: 17637737.

763 4. Hurley JH. ESCRTs are everywhere. EMBO J. 2015;34(19):2398-407. doi:
764 10.15252/embj.201592484. PubMed PMID: 26311197; PubMed Central PMCID:
765 PMCPMC4601661.

766 5. Schmidt O, Teis D. The ESCRT machinery. Curr Biol. 2012;22(4):R116-20. doi:
767 10.1016/j.cub.2012.01.028. PubMed PMID: 22361144; PubMed Central PMCID:
768 PMCPMC3314914.

769 6. Shim JH, Xiao C, Hayden MS, Lee KY, Trombetta ES, Pypaert M, et al. CHMP5 is
770 essential for late endosome function and down-regulation of receptor signaling during mouse
771 embryogenesis. J Cell Biol. 2006;172(7):1045-56. doi: 10.1083/jcb.200509041. PubMed PMID:
772 16567502; PubMed Central PMCID: PMCPMC2063762.

773 7. Kranz A, Kinner A, Kolling R. A family of small coiled-coil-forming proteins functioning
774 at the late endosome in yeast. Mol Biol Cell. 2001;12(3):711-23. Epub 2001/03/17. doi:
775 10.1091/mbc.12.3.711. PubMed PMID: 11251082; PubMed Central PMCID: PMCPMC30975.

776 8. Greenblatt MB, Park KH, Oh H, Kim JM, Shin DY, Lee JM, et al. CHMP5 controls bone
777 turnover rates by dampening NF-kappaB activity in osteoclasts. J Exp Med. 2015;212(8):1283-

778 301. Epub 20150720. doi: 10.1084/jem.20150407. PubMed PMID: 26195726; PubMed Central
779 PMCID: PMCPMC4516796.
780 9. Adoro S, Park KH, Bettigole SE, Lis R, Shin HR, Seo H, et al. Post-translational control
781 of T cell development by the ESCRT protein CHMP5. Nat Immunol. 2017;18(7):780-90. doi:
782 10.1038/ni.3764. PubMed PMID: 28553951.
783 10. Parenti G, Medina DL, Ballabio A. The rapidly evolving view of lysosomal storage
784 diseases. EMBO Mol Med. 2021;13(2):e12836. Epub 20210118. doi:
785 10.15252/emmm.202012836. PubMed PMID: 33459519; PubMed Central PMCID:
786 PMCPMC7863408.
787 11. Morishita K, Petty RE. Musculoskeletal manifestations of mucopolysaccharidoses.
788 Rheumatology (Oxford). 2011;50 Suppl 5:v19-25. Epub 2012/01/11. doi:
789 10.1093/rheumatology/ker397. PubMed PMID: 22210666.
790 12. Clarke LA, Hollak CE. The clinical spectrum and pathophysiology of skeletal
791 complications in lysosomal storage disorders. Best Pract Res Clin Endocrinol Metab.
792 2015;29(2):219-35. Epub 20140827. doi: 10.1016/j.beem.2014.08.010. PubMed PMID: 25987175.
793 13. Miller BS, Fung EB, White KK, Lund TC, Harmatz P, Orchard PJ, et al. Persistent bone
794 and joint disease despite current treatments for mucopolysaccharidosis types I, II, and VI: Data
795 from a 10-year prospective study. J Inherit Metab Dis. 2023;46(4):695-704. Epub 20230306. doi:
796 10.1002/jimd.12598. PubMed PMID: 36840680; PubMed Central PMCID: PMCPMC10824391.
797 14. Yang W, Wang J, Moore DC, Liang H, Dooner M, Wu Q, et al. Ptpn11 deletion in a novel
798 progenitor causes metachondromatosis by inducing hedgehog signalling. Nature.
799 2013;499(7459):491-5. doi: 10.1038/nature12396. PubMed PMID: 23863940; PubMed Central
800 PMCID: PMCPMC4148013.

801 15. Debnath S, Yallowitz AR, McCormick J, Lalani S, Zhang T, Xu R, et al. Discovery of a
802 periosteal stem cell mediating intramembranous bone formation. Nature. 2018;562(7725):133-9.
803 Epub 2018/09/27. doi: 10.1038/s41586-018-0554-8. PubMed PMID: 30250253; PubMed Central
804 PMCID: PMCPMC6193396.
805 16. Shi R, He L, Ren J, Zhou B, Hou G, Zhou B, et al. A migratory stem cell population for
806 musculoskeletal enveloping tissues and the bone. SSRN 3281656, 2018.
807 2018;(http://dx.doi.org/10.2139/ssrn.3281656). doi: 10.2139/ssrn.3281656.
808 17. Logan M, Martin JF, Nagy A, Lobe C, Olson EN, Tabin CJ. Expression of Cre
809 Recombinase in the developing mouse limb bud driven by a Prxl enhancer. Genesis.
810 2002;33(2):77-80. doi: 10.1002/gene.10092. PubMed PMID: 12112875.
811 18. Ono N, Ono W, Mizoguchi T, Nagasawa T, Frenette PS, Kronenberg HM. Vasculature-
812 associated cells expressing nestin in developing bones encompass early cells in the osteoblast and
813 endothelial lineage. Dev Cell. 2014;29(3):330-9. Epub 2014/05/16. doi:
814 10.1016/j.devcel.2014.03.014. PubMed PMID: 24823376; PubMed Central PMCID:
815 PMCPMC4083679.
816 19. Maes C, Kobayashi T, Selig MK, Torrekens S, Roth SI, Mackem S, et al. Osteoblast
817 precursors, but not mature osteoblasts, move into developing and fractured bones along with
818 invading blood vessels. Dev Cell. 2010;19(2):329-44. doi: 10.1016/j.devcel.2010.07.010. PubMed
819 PMID: 20708594; PubMed Central PMCID: PMCPMC3540406.
820 20. Lim J, Shi Y, Karner CM, Lee SY, Lee WC, He G, et al. Dual function of Bmpr1a signaling
821 in restricting preosteoblast proliferation and stimulating osteoblast activity in mouse. Development.
822 2016;143(2):339-47. doi: 10.1242/dev.126227. PubMed PMID: 26657771; PubMed Central
823 PMCID: PMCPMC4725340.

824 21. Lim J, Burclaff J, He G, Mills JC, Long F. Unintended targeting of Dmp1-Cre reveals a
825 critical role for Bmpr1a signaling in the gastrointestinal mesenchyme of adult mice. Bone Res.
826 2017;5:16049. doi: 10.1038/boneres.2016.49. PubMed PMID: 28163952; PubMed Central
827 PMCID: PMCPMC5282469.
828 22. Matic I, Matthews BG, Wang X, Dyment NA, Worthley DL, Rowe DW, et al. Quiescent
829 Bone Lining Cells Are a Major Source of Osteoblasts During Adulthood. Stem Cells.
830 2016;34(12):2930-42. Epub 2016/08/11. doi: 10.1002/stem.2474. PubMed PMID: 27507737;
831 PubMed Central PMCID: PMCPMC5450652.
832 23. Ge X, Tsang K, He L, Garcia RA, Ermann J, Mizoguchi F, et al. NFAT restricts
833 osteochondroma formation from entheseal progenitors. JCI Insight. 2016;1(4):e86254. doi:
834 10.1172/jci.insight.86254. PubMed PMID: 27158674; PubMed Central PMCID:
835 PMCPMC4855520.
836 24. Birch J, Gil J. Senescence and the SASP: many therapeutic avenues. Genes Dev.
837 2020;34(23-24):1565-76. Epub 2020/12/03. doi: 10.1101/gad.343129.120. PubMed PMID:
838 33262144; PubMed Central PMCID: PMCPMC7706700.
839 25. Romanello M, Piatkowska E, Antoniali G, Cesaratto L, Vascotto C, Iozzo RV, et al.
840 Osteoblastic cell secretome: a novel role for progranulin during risedronate treatment. Bone.
841 2014;58:81-91. Epub 2013/10/15. doi: 10.1016/j.bone.2013.10.003. PubMed PMID: 24120669;
842 PubMed Central PMCID: PMCPMC5072534.
843 26. Davies OG, Cox SC, Azoidis I, McGuinness AJA, Cooke M, Heaney LM, et al. Osteoblast-
844 Derived Vesicle Protein Content Is Temporally Regulated During Osteogenesis: Implications for
845 Regenerative Therapies. Front Bioeng Biotechnol. 2019;7:92. Epub 20190501. doi:

846 10.3389/fbioe.2019.00092. PubMed PMID: 31119130; PubMed Central PMCID:
847 PMCPMC6504811.
848 27. Zhu Y, Tchkonia T, Pirtskhalava T, Gower AC, Ding H, Giorgadze N, et al. The Achilles'
849 heel of senescent cells: from transcriptome to senolytic drugs. Aging Cell. 2015;14(4):644-58.
850 Epub 2015/03/11. doi: 10.1111/acel.12344. PubMed PMID: 25754370; PubMed Central PMCID:
851 PMCPMC4531078.
852 28. Hickson LJ, Langhi Prata LGP, Bobart SA, Evans TK, Giorgadze N, Hashmi SK, et al.
853 Senolytics decrease senescent cells in humans: Preliminary report from a clinical trial of Dasatinib
854 plus Quercetin in individuals with diabetic kidney disease. EBioMedicine. 2019;47:446-56. Epub
855 2019/09/23. doi: 10.1016/j.ebiom.2019.08.069. PubMed PMID: 31542391; PubMed Central
856 PMCID: PMCPMC6796530.
857 29. Martini H, Passos JF. Cellular senescence: all roads lead to mitochondria. FEBS J.
858 2023;290(5):1186-202. Epub 20220130. doi: 10.1111/febs.16361. PubMed PMID: 35048548;
859 PubMed Central PMCID: PMCPMC9296701.
860 30. Park JT, Lee YS, Cho KA, Park SC. Adjustment of the lysosomal-mitochondrial axis for
861 control of cellular senescence. Ageing Res Rev. 2018;47:176-82. Epub 20180821. doi:
862 10.1016/j.arr.2018.08.003. PubMed PMID: 30142381.
863 31. Gorgoulis V, Adams PD, Alimonti A, Bennett DC, Bischof O, Bishop C, et al. Cellular
864 Senescence: Defining a Path Forward. Cell. 2019;179(4):813-27. Epub 2019/11/02. doi:
865 10.1016/j.cell.2019.10.005. PubMed PMID: 31675495.
866 32. Korolchuk VI, Miwa S, Carroll B, von Zglinicki T. Mitochondria in Cell Senescence: Is
867 Mitophagy the Weakest Link? EBioMedicine. 2017;21:7-13. Epub 2017/03/24. doi:

868 10.1016/j.ebiom.2017.03.020. PubMed PMID: 28330601; PubMed Central PMCID:
869 PMCPMC5514379.
870 33. Birch J, Passos JF. Targeting the SASP to combat ageing: Mitochondria as possible
871 intracellular allies? Bioessays. 2017;39(5). Epub 2017/02/22. doi: 10.1002/bies.201600235.
872 PubMed PMID: 28217839.
873 34. Paramos-de-Carvalho D, Jacinto A, Saude L. The right time for senescence. Elife. 2021;10.
874 Epub 2021/11/11. doi: 10.7554/eLife.72449. PubMed PMID: 34756162; PubMed Central PMCID:
875 PMCPMC8580479.
876 35. Wiley CD, Campisi J. The metabolic roots of senescence: mechanisms and opportunities
877 for intervention. Nat Metab. 2021;3(10):1290-301. Epub 2021/10/20. doi: 10.1038/s42255-021-
878 00483-8. PubMed PMID: 34663974; PubMed Central PMCID: PMCPMC8889622.
879 36. Martini H, Passos JF. Cellular senescence: all roads lead to mitochondria. FEBS J. 2022.
880 Epub 2022/01/21. doi: 10.1111/febs.16361. PubMed PMID: 35048548; PubMed Central PMCID:
881 PMCPMC9296701.
882 37. Vild CJ, Li Y, Guo EZ, Liu Y, Xu Z. A novel mechanism of regulating the ATPase VPS4
883 by its cofactor LIP5 and the endosomal sorting complex required for transport (ESCRT)-III protein
884 CHMP5. J Biol Chem. 2015;290(11):7291-303. doi: 10.1074/jbc.M114.616730. PubMed PMID:
885 25637630; PubMed Central PMCID: PMCPMC4358147.
886 38. Yang Z, Vild C, Ju J, Zhang X, Liu J, Shen J, et al. Structural basis of molecular recognition
887 between ESCRT-III-like protein Vps60 and AAA-ATPase regulator Vta1 in the multivesicular
888 body pathway. J Biol Chem. 2012;287(52):43899-908. Epub 2012/10/30. doi:
889 10.1074/jbc.M112.390724. PubMed PMID: 23105107; PubMed Central PMCID:
890 PMCPMC3527972.

891 39. Rodger C, Flex E, Allison RJ, Sanchis-Juan A, Hasenahuer MA, Cecchetti S, et al. De
892 Novo VPS4A Mutations Cause Multisystem Disease with Abnormal Neurodevelopment. Am J
893 Hum Genet. 2020;107(6):1129-48. Epub 20201112. doi: 10.1016/j.ajhg.2020.10.012. PubMed
894 PMID: 33186545; PubMed Central PMCID: PMCPMC7820634.
895 40. Salazar JC, Duhnam-Ems S, La Vake C, Cruz AR, Moore MW, Caimano MJ, et al.
896 Activation of human monocytes by live Borrelia burgdorferi generates TLR2-dependent and -
897 independent responses which include induction of IFN-beta. PLoS Pathog. 2009;5(5):e1000444.
898 Epub 2009/05/23. doi: 10.1371/journal.ppat.1000444. PubMed PMID: 19461888; PubMed
899 Central PMCID: PMCPMC2679197.
900 41. Thiebaut R, Esmiol S, Lecine P, Mahfouz B, Hermant A, Nicoletti C, et al. Characterization
901 and Genetic Analyses of New Genes Coding for NOD2 Interacting Proteins. PLoS One.
902 2016;11(11):e0165420. Epub 2016/11/05. doi: 10.1371/journal.pone.0165420. PubMed PMID:
903 27812135; PubMed Central PMCID: PMCPMC5094585.
904 42. Lu Y, Xie Y, Zhang S, Dusevich V, Bonewald LF, Feng JQ. DMP1-targeted Cre
905 expression in odontoblasts and osteocytes. J Dent Res. 2007;86(4):320-5. doi:
906 10.1177/154405910708600404. PubMed PMID: 17384025.
907 43. Rodda SJ, McMahon AP. Distinct roles for Hedgehog and canonical Wnt signaling in
908 specification, differentiation and maintenance of osteoblast progenitors. Development.
909 2006;133(16):3231-44. doi: 10.1242/dev.02480. PubMed PMID: 16854976.
910 44. Nakamura T, Imai Y, Matsumoto T, Sato S, Takeuchi K, Igarashi K, et al. Estrogen
911 prevents bone loss via estrogen receptor alpha and induction of Fas ligand in osteoclasts. Cell.
912 2007;130(5):811-23. doi: 10.1016/j.cell.2007.07.025. PubMed PMID: 17803905.

913 45. Bonetto A, Andersson DC, Waning DL. Assessment of muscle mass and strength in mice.
914 Bonekey Rep. 2015;4:732. doi: 10.1038/bonekey.2015.101. PubMed PMID: 26331011; PubMed
915 Central PMCID: PMCPMC4549925.
916 46. Takeshita H, Yamamoto K, Nozato S, Inagaki T, Tsuchimochi H, Shirai M, et al. Modified
917 forelimb grip strength test detects aging-associated physiological decline in skeletal muscle
918 function in male mice. Sci Rep. 2017;7:42323. doi: 10.1038/srep42323. PubMed PMID: 28176863;
919 PubMed Central PMCID: PMCPMC5296723.
920 47. Langmead B, Salzberg SL. Fast gapped-read alignment with Bowtie 2. Nat Methods.
921 2012;9(4):357-9. Epub 2012/03/06. doi: 10.1038/nmeth.1923. PubMed PMID: 22388286;
922 PubMed Central PMCID: PMCPMC3322381.
923 48. Dobin A, Davis CA, Schlesinger F, Drenkow J, Zaleski C, Jha S, et al. STAR: ultrafast
924 universal RNA-seq aligner. Bioinformatics. 2013;29(1):15-21. Epub 2012/10/30. doi:
925 10.1093/bioinformatics/bts635. PubMed PMID: 23104886; PubMed Central PMCID:
926 PMCPMC3530905.
927 49. Trapnell C, Hendrickson DG, Sauvageau M, Goff L, Rinn JL, Pachter L. Differential
928 analysis of gene regulation at transcript resolution with RNA-seq. Nat Biotechnol. 2013;31(1):46-
929 53. Epub 2012/12/12. doi: 10.1038/nbt.2450. PubMed PMID: 23222703; PubMed Central PMCID:
930 PMCPMC3869392.
931 50. Fabregat A, Sidiropoulos K, Viteri G, Forner O, Marin-Garcia P, Arnau V, et al. Reactome
932 pathway analysis: a high-performance in-memory approach. BMC Bioinformatics.
933 2017;18(1):142. Epub 2017/03/03. doi: 10.1186/s12859-017-1559-2. PubMed PMID: 28249561;
934 PubMed Central PMCID: PMCPMC5333408.

935 51. Schmittgen TD, Livak KJ. Analyzing real-time PCR data by the comparative C(T) method.
936 Nat Protoc. 2008;3(6):1101-8. Epub 2008/06/13. doi: 10.1038/nprot.2008.73. PubMed PMID:
937 18546601.
938 52. Fiorese CJ, Schulz AM, Lin YF, Rosin N, Pellegrino MW, Haynes CM. The Transcription
939 Factor ATF5 Mediates a Mammalian Mitochondrial UPR. Curr Biol. 2016;26(15):2037-43. doi:
940 10.1016/j.cub.2016.06.002. PubMed PMID: 27426517; PubMed Central PMCID:
941 PMCPMC4980197.
942

943 ## Figure Legends

944 **Fig. 1. Ablation of *Chmp5* in mouse osteogenic lineage cells causes aberrant bone**
945 **formation.**

946 (**A**) Micro-CT and H&E staining showing periskeletal overgrowth in *Chmp5*^{Ctsk} mice in
947 comparison with *Chmp5*$^{fl/fl}$ mice at 7 weeks of age. Dot line representing the approximate
948 bone border. *n* = 10 animals per group. (**B**) Micro-CT images displaying periskeletal
949 overgrowth in the ankle and foot in *Chmp5*^{Ctsk} versus *Chmp5*$^{fl/fl}$ mice at one year of age.
950 *n* = 4 animals per group. (**C**) Alizarin red staining of skeletal preparations on postnatal
951 day 10. *n* = 4 mice per group, arrows indicating periskeletal bone overgrowth. (**D**) Three-
952 point test showing femur bone stiffness and ultimate stress (fracture stress) in *Chmp5*^{Ctsk}
953 and *Chmp5*$^{fl/fl}$ mice. *n* = 5 male animals per group. Similar changes observed in both
954 sexes. (**E**) Confocal images mapping *Ctsk*$^{+}$ (GFP^{+}) progenitors in periskeletal tissues in
955 *Chmp5*$^{Ctsk/+}$;*Rosa26*$^{mTmG/+}$ and *Chmp5*^{Ctsk};*Rosa26*$^{mTmG/+}$ mice at 2 weeks of age.
956 Asterisks indicating periskeletal overgrowths; dot-line representing the approximate bone
957 border. *n* = 4 animals each group. (**F**) X-ray images demonstrating progressive cortical
958 bone expansion (arrows) and decreased skeletal muscle mass (asterisks) in *Chmp5*^{Dmp1}
959 in comparison with *Chmp5*$^{fl/fl}$ mice. *n* = 3, 3, 10, 8 animals per group for 3 weeks, 5 weeks,
960 10 weeks, and 1 year of age, respectively. (**G**) Micro-CT analyses displaying cortical bone
961 expansion in *Chmp5*^{Dmp1} relative to *Chmp5*$^{fl/fl}$ mice at 10 weeks of age. *n* = 6 *Chmp5*$^{fl/fl}$
962 and 5 *Chmp5*^{Dmp1} male mice, similar changes found in both genders. (**H**) Skeletal muscle
963 mass in *Chmp5*^{Dmp1} compared to *Chmp5*$^{fl/fl}$ mice at 10-12 weeks of age. *n* = 4 animals
964 (male) per group, similar changes found in both genders. (**I**) Hindlimb abduction of
965 *Chmp5*^{Dmp1} mice in comparison with *Chmp5*$^{fl/fl}$ littermate controls at 10 weeks of age.

966 More than 20 animals per group observed. (**J**) Four-limb handing time (*n* = 10 per group,
967 pooled data from both sexes), and forelimb pull strength (*n* = 6 per group, male mice) in
968 *Chmp5*^{Dmp1} compared to *Chmp5*$^{fl/fl}$ mice at 10-12 weeks of age. Similar changes found
969 in both genders. All data are mean ± s.d.; two-tailed unpaired Student's *t*-test. Scale bars,
970 1 mm for micro-CT and skeletal preparation images, 200 μm for histological images, and
971 10 mm in panel (**F**).
972
973 **Fig. 2. CHMP5 restricts osteogenesis in skeletal progenitor cells.**
974 (**A**) Flow cytometry showing the strategy for sorting CD45$^-$;CD31$^-$;GFP$^+$ and
975 CD45$^-$;CD31$^-$;GFP$^-$ periskeletal progenitors from periskeletal tissues of
976 *Chmp5*$^{Ctsk/+}$;*Rosa26*$^{mTmG/+}$ and *Chmp5*^{Ctsk};*Rosa26*$^{mTmG/+}$ mice at 2 weeks of age. *n* = 10
977 mice per group. (**B**) Quantitative PCR determining the expression of *Chmp5* in *Chmp5*^{Ctsk}
978 relative to *Chmp5*$^{Ctsk/+}$ periskeletal progenitors. *n* = 6 mice per group. (**C**) Alizarin red
979 staining, von Kossa staining and alkaline phosphatase activity assay determining
980 osteogenesis in *Chmp5*^{Ctsk} compared to *Chmp5*$^{Ctsk/+}$ periskeletal progenitors. *n* = 3
981 replicates each group, representative results of cells from 3 different mice per group. (**D**)
982 Western blot confirming *Chmp5* deletion in mouse MC3T3-E1 cells by lentiviral
983 CRISPR/CAS9. (**E**) Alizarin red staining demonstrating osteogenesis in MC3T3-E1 cells
984 with or without *Chmp5* deletion by lentiviral CRISPR/CAS9. *n* = 4 replicates per group,
985 experiments repeated twice for each time point. **(F)** Ingenuity pathway analysis of RNA-
986 seq data showing increased activity of osteoblast differentiation in *Chmp5*^{Ctsk} vs.
987 *Chmp5*$^{Ctsk/+}$ periskeletal progenitors. All data are mean ± s.d.; two-tailed unpaired
988 Student's *t*-test.

989

990 **Fig. 3. CHMP5 controls skeletal progenitor cell senescence.**

991 (**A**) Cell number counting and AlamarBlue assay determining cell proliferation in
992 *Chmp5*^{Ctsk} and *Chmp5*$^{Ctsk/+}$ periskeletal progenitors from 2-week-old animals. *n* = 3
993 replicates per group per time point; experiments repeated 3 times using cells from 3
994 different mice. (**B**) Volcano plot of RNA-seq data showing differentially expressed genes
995 in *Chmp5*^{Ctsk} vs. *Chmp5*$^{Ctsk/+}$ periskeletal progenitors. *n* = 3 per group with cells from 3
996 different animals. (**C**) ConsensusPathDB gene set enrichment analysis of RNA-seq data
997 showing positive enrichment of genes in multiple molecular pathways related to cell
998 senescence in *Chmp5*^{Ctsk} relative to *Chmp5*$^{Ctsk/+}$ periskeletal progenitors. (**D**) Western blot
999 determining the expression of p16 and p21 proteins in *Chmp5*^{Ctsk} compared to *wild-type*
1000 (control) periskeletal progenitors. The numbers above lanes indicating the intensity of the
1001 p16 or p21 band relative to that of *Control* cells after normalization by β-Actin. Results
1002 repeated 3 times with cells from 3 different animals. (**E**) Gross image demonstrating
1003 aging-related phenotypes in *Chmp5*^{Ctsk} compared to *Chmp5*$^{Ctsk/+}$ mice at 1 year of age.
1004 Images are representative of 5 animals per group. (**F**) Western blot confirming deletion of
1005 *Chmp5* in ATDC5 cells by lentiviral CRISPR/CAS9. (**G**) Cell cycle analysis in ATDC5 cells
1006 with or without *Chmp5* deletion. *n* = 3 replicates per group, results repeated twice. All data
1007 are mean ± s.d.; 2-way ANOVA followed by multiple comparisons.

1008

1009 **Fig. 4. Secretory phenotype of *Chmp5*-deficient skeletal progenitors.**

1010 (**A**) GSEA of RNA-seq data showing positive enrichment of genes associated with the
1011 molecular pathway of senescence-associated secretory phenotype (Reactome database)

1012 in *Chmp5*^{Ctsk} relative to *Chmp5*$^{Ctsk/+}$ periskeletal progenitors. (**B**) Confocal images
1013 showing and quantifying extracellular vesicles (arrowheads) around *Chmp5*^{Ctsk}
1014 periskeletal progenitors. Images are representative of 30 cells from 3 animals per group.
1015 Scale bars, 10 μm. (**C** and **D**) Nanoparticle tracking analysis of extracellular vesicles in
1016 culture medium of *Chmp5*^{Ctsk} and *wild-type* periskeletal progenitors. Data pooled from 3
1017 replicates per group, 5 reads for each; repeated twice using cells from 2 mice per group.
1018 (**E**) Cell number counting determining cell proliferation in ATDC5 cells treated with culture
1019 supernatant from *Chmp5*-deficient or *Chmp5*-sufficient cells. *n* = 3 per group per time
1020 point, repeated twice. (**F** and **G**) Cell number counting and alizarin red staining examining
1021 cell proliferation (**F**) and osteogenesis (**G**) in neighboring CD45^{-};CD31^{-};GFP^{-} progenitors
1022 sorted from periskeletal tissues of *Chmp5*^{Ctsk}*;Rosa26*$^{mTmG/+}$ or *Ctsk-Cre;Rosa26*$^{mTmG/+}$
1023 mice. *n* = 3 replicates per group per time point, repeated 3 times using cells from 3
1024 different animals. (**H**) Volcano plot showing differentially secreted protein in supernatants
1025 of *Chmp5*^{Ctsk} vs. *wild-type* periskeletal progenitors analyzed by Nano LC-MS/MS. *n* = 3
1026 with cells from 3 different animals per group. (**I**) Western blot verifying the increase in
1027 COL1A1 and TAGLN proteins in supernatants of *Chmp5*^{Ctsk} relative to *wild-type*
1028 periskeletal progenitors. Commas blue stain as the loading control. Results repeated 3
1029 times using cells from 3 different mice each group. All data are mean ± s.d.; two-tailed
1030 unpaired Student's *t*-test for comparison of two groups or 2-way ANOVA followed by
1031 multiple comparisons.
1032

1033 **Fig. 5. Senolytic treatment mitigates musculoskeletal pathologies in *Chmp5***
1034 **conditional knockout mice.**

1035 (**A**) Incucyte live-cell apoptosis analysis of *Chmp5*^{Ctsk} and *wild-type* periskeletal
1036 progenitors treated with 50 μM Quercetin and 500 nM dasatinib (Q + D) and labeled by
1037 Annexin V. *n* = 6 for each group, experiment repeated twice using cells from different
1038 animals. (**B**) Gross images, radiography, and histology (H&E) respectively demonstrating
1039 hindlimb abduction and periskeletal bone overgrowth (arrows or dot-line) in *Chmp5*^{Ctsk} in
1040 comparison with *Chmp5*$^{fl/fl}$ mice after treatment with Q + D or vehicle PEG400 weekly for
1041 7 weeks. *n* = 8-10 mice per group. Continuous lines in H&E images indicating an
1042 approximate edge of the cortical bone and dot lines indicating the edge of periskeletal
1043 overgrowing bones. Scale bars, 100 μm. (**C**) Four-limb hanging time and forelimb pull
1044 strength in *Chmp5*^{Dmp1} and *Chmp5*$^{fl/fl}$ mice after treatment with Q + D or the vehicle
1045 PEG400. *n* = 12 animals per group for hanging time test pooled from both genders; *n* = 7
1046 male mice per group for the forelimb pull strength test, similar changes found in both
1047 genders. (**D**) Gross images showing hindlimb abduction in *Chmp5*^{Dmp1} compared to
1048 *Chmp5*$^{fl/fl}$ mice after treatment with Q + D or the vehicle PEG400. *n* = 12 animals per
1049 group. (**E**) Micro-CT analysis demonstrating cortical bone thickness in *Chmp5*^{Dmp1} mice
1050 after treatment with Q + D or the vehicle PEG400. *n* = 5 male mice per group, similar
1051 changes found in both genders. All data are mean ± s.d.; 2-way ANOVA followed by
1052 multiple comparisons or two-tailed unpaired Student's *t*-test for comparison of two groups.
1053
1054 **Fig. 6. CHMP5 is essential for endolysosomal functions and maintaining VPS4A**
1055 **protein in skeletal progenitors.**
1056

1057 (**A**) Representative confocal images demonstrating abnormally enlarged vesicles in
1058 cultured *Chmp5*^{Ctsk} relative to *wild-type* periskeletal progenitors. Abnormal cells identified
1059 by containing enlarged GFP^{+} vesicles. *n* = 200 cells from 3 mice per group. (**B**) Schematic
1060 showing molecular markers utilized to analyze the endocytic pathway. (**C**) Representative
1061 confocal images showing LAMP1 immunostaining in *Chmp5*^{Ctsk} and *wild-type* periskeletal
1062 progenitors. *n* = 20 cells per group. (**D**) Quantification of LAMP1^{+} vesicles in ATDC5 cells
1063 with or without *Chmp5* depletion. *n* = 93, 66 cells, respectively. (**E**) Representative
1064 confocal images showing RAB7 immunostaining in *Chmp5*^{Ctsk} and *wild-type* periskeletal
1065 progenitors. *n* = 15 cells per genotype. (**F**) Quantification of RAB7^{+} vesicles in ATDC5
1066 cells with or without *Chmp5* depletion. *n* = 94, 92 cells, respectively. (**G)** Transmission
1067 electron microscopy showing the accumulation of multivesicular body-like structures
1068 (arrows) and lysosome-like structures (arrowheads) in *Chmp5*^{Ctsk} relative to *wild-type*
1069 periskeletal progenitors. *n* = 30 cells per group. (**H**) Confocal live cell images
1070 demonstrating delayed degradation of the EGF conjugate in *Chmp5*^{Ctsk} vs. *wild-type*
1071 periskeletal progenitors. *n* = 10 cells each group per time point. (**I**) Volcano plot of
1072 proteomic analysis showing differentially expressed proteins in *Chmp5*^{Ctsk} vs. *wild-type*
1073 periskeletal progenitors. *n* = 3 with cells from 3 different animals. (**J**) Western blot verifying
1074 the decrease in VPS4A protein in *Chmp5*^{Ctsk} vs. *wild-type* periskeletal progenitors. The
1075 numbers above lanes indicating the intensity of the VPS4A band relative to that of *wild-*
1076 *type* cells after normalization by β-Actin. Results repeated 3 times with cells from 3
1077 different mice each group. All data are mean ± s.d.; Mann-Whitney test for the comparison
1078 of the vesicle number and two-tailed unpaired Student's *t*-test for the comparison of the
1079 vesicle size in (**D**) and (**F**). Scale bars, 10 μm except (**G**) as indicated.

1080

1081 **Fig. 7. Mitochondrial dysfunction is responsible for cell senescence in *Chmp5*-**
1082 **deleted skeletal progenitors.**

1083 (**A**) GSEA of RNA--seq data reporting positive enrichment of genes associated with the
1084 molecular pathway of oxidative stress-induced senescence in *Chmp5*^{Ctsk} relative to
1085 *Chmp5*$^{Ctsk/+}$ periskeletal progenitors. (**B**) Confocal fluorescence images showing
1086 intracellular ROS (CellROX Deep Red) and mitochondria (TMRE) in *Chmp5*^{Ctsk} vs. *wild-*
1087 *type* periskeletal progenitors. Images are representative of 30 cells per group. Scale bars,
1088 15 μm. The graph on the right shows the quantification of the fluorescence intensity of
1089 CellROX Deep Red. *n* = 10 each group, results repeated twice. (**C**) Quantification of
1090 TMRE fluorescence intensity in *Chmp5*-sufficient and *Chmp5*-deficient ATDC5 cells. *n* =
1091 12 for each group, repeated 3 times. (**D**) Western blotting determining the expression of
1092 mitochondrial OXPHOS proteins NDUF88, SDHB, MT-CO1, UQCRC2, and ATF5A in
1093 *Chmp5*-deficient compared to *Chmp5*-sufficient ATDC5 cells. Experiment repeated twice.
1094 (**E**) Cell number counting to determine cell proliferation in galactose medium. *n* = 6
1095 replicates per group, repeated three times. (**F**) Seahorse mitochondrial stress test
1096 showing mitochondrial respiratory capacity and extracellular acidification rate in
1097 *Chmp5*^{Ctsk} relative to *wild-type* periskeletal progenitors. Data pooled from cells of 3 mice,
1098 8 replicates for each sample. (**G**) Cell number counting and AlamarBlue assay
1099 determining cell proliferation in ATDC5 cells with or without *Chmp5* depletion after
1100 treatment with the antioxidant *N*-Acetyl cysteine. *n* = 3 or 12 each group for cell number
1101 counting or AlamarBlue assay, respectively; results repeated 3 times. (**H**) Schematic
1102 showing the function of CHMP5 in maintaining VPS4A protein and endolysosomal

1103 homeostasis and restricting cell senescence and osteogenesis in skeletal progenitors. All

1104 data are mean ± s.d.; two-tailed unpaired Student's *t*-test, except the Mann-Whitney test

1105 in panel (**E**).

1106

1107 ## Supplementary Figure Legends

1108 **Fig. S1. CHMP5 restricts bone formation in osteogenic lineage cells.**

1109 (**A**) Alizarin red staining of skeletal preparations on postnatal day 2. *n* = 4 mice per group.
1110 Scale bar, 1 mm. (**B**) Confocal images of *Rosa26*$^{mTmG/+}$ (Cre^{-}) control mice. Related to
1111 Fig. 1E. Scale bar, 200 μm. (**C**) Tartrate-resistant acid phosphatase (TRAP) staining
1112 demonstrating the absence of osteoclasts in peri-skeletal overgrowth (asterisk) of
1113 *Chmp5*^{Ctsk} mice at 2 weeks of age. TRAP^{+} osteoclasts in the bone marrow as positive
1114 control; dot-line representing approximate border between peri-skeletal overgrowth and
1115 the bone at femoral condyle of the knee. Images are representative of 3 animals per group.
1116 Scale bar, 200 μm. (**D**) Gross image and measurement of femur thickness showing bone
1117 expansion in *Chmp5*^{Dmp1} versus *Chmp5*$^{fl/fl}$ mice at 10 weeks of age. *n* = 13 *Chmp5*$^{fl/fl}$ and
1118 12 *Chmp5*^{Dmp1} mice. Scale bar, 1 mm. (**E**) H&E histology showing bone expansion at the
1119 endosteum (arrows) in *Chmp5*^{Dmp1} mice. The left images showing the midshaft and the
1120 right images showing the metaphysis of the femur bone. Images are representative of 3
1121 mice per group. Scale bars, 0.5 mm. Data are mean ± s.d.; two-tailed unpaired Student's
1122 *t*-test.

1123

1124 **Fig. S2. Sorting of CD45^{-};CD31^{-};CTSK^{+} periskeletal progenitors.**

1125 (**A**) Unstained cells from *Rosa26-mTmG*$^{fl/+}$ mice as a negative control for sorting
1126 CD45^{-};CD31^{-};CTSK^{+} skeletal progenitors. Related to Fig. 2A. (**B**) Quantification of
1127 CD45^{-};CD31^{-};GFP^{+} and CD45^{-};CD31^{-};GFP^{-} cell population in samples of
1128 *Chmp5*^{Ctsk}*;Rosa26*$^{mTmG/+}$ mice. *n* = 10 mice per group.

1129

1130 **Fig. S3. Cell apoptosis is not the main cause of the decreased proliferative rate in**
1131 ***Chmp5*-deficient skeletal progenitors.**
1132 (**A**) Annexin V stain examining cellular apoptosis in *Chmp5*^{Ctsk} and *Chmp5*$^{Ctsk/+}$
1133 periskeletal progenitors. *n* = 3 replicates each group; repeated twice using cells from 2
1134 mice per group. (**B**) TUNEL staining and quantification of TUNEL^{+} cells (%) in the
1135 periskeletal tissues of *Chmp5*^{Ctsk} and *Chmp5*$^{Ctsk/+}$ mice. Arrows indicating positive cells in
1136 periskeletal overgrowth in *Chmp5*^{Ctsk} mice, dot-line representing approximate border
1137 between periskeletal overgrowth and bone in the femoral condyle of the knee; *n* = 3
1138 animals per group; scale bars, 100 μm. (**C**) Cell number counting determining cell
1139 proliferation in ATDC5 cells after deleting *Chmp5* by lentiviral CRISPR/CAS9. *n* = 4
1140 replicates per group per time point, experiment repeated three times. (**D**) Annexin V-PI
1141 stain analyzing cellular apoptosis in ATDC5 cells with or without *Chmp5* deletion. *n* = 3
1142 replicates for each group, repeated 3 times. (**E**) Cell number counting determining cell
1143 proliferation in ATDC5 cells with or without *Chmp5* deletion after treatment with the pan-
1144 caspase inhibitor Q-VD-OPh. *n* = 3 replicates of each group each dose, repeated twice.
1145 All data are mean ± s.d.; two-tailed Student's *t*-test for comparison of two groups or 2-
1146 way ANOVA followed by multiple comparisons.
1147
1148 **Fig. S4. Secretory phenotype of *Chmp5*-deficient skeletal progenitors.**
1149 (**A**) Nanoparticle tracking analysis showing the size distribution of extracellular vesicles
1150 in *Chmp5*^{Ctsk} and *wild-type* skeletal progenitors. Data pooled from 3 replicates, 5 reads
1151 for each; repeated twice using cells from 2 mice; D10, D50, and D90 indicating percent
1152 undersize, for example D50 = 229 nm representing that 50% of vesicles are 229 nm or

1153 smaller. (**B**) AlarmaBlue assay examining cell proliferation in neighboring
1154 CD45$^-$;CD31$^-$;GFP$^-$ progenitors sorted from periskeletal tissues of
1155 *Chmp5^{Ctsk};Rosa26$^{mTmG/+}$* or *Ctsk-Cre;Rosa26$^{mTmG/+}$* mice. *n* = 12 replicates per group per
1156 time-point, repeated 3 times using cells from 3 animals. (**C**) Alizarin red staining
1157 determining osteogenesis in neighboring CD45$^-$;CD31$^-$;GFP$^-$ progenitors sorted from
1158 periskeletal tissues of *Chmp5^{Ctsk};Rosa26$^{mTmG/+}$* or *Ctsk-Cre;Rosa26$^{mTmG/+}$* mice after
1159 induction in osteogenic medium for 3 weeks. *n* = 3 replicates per group per time point,
1160 repeated 3 times using cells from 3 animals. (**D**) Immunostaining and quantification of cell
1161 proliferation marker Ki-67 in the periskeletal tissues around the knee of *Chmp5^{Ctsk}* and
1162 *Chmp5$^{Ctsk/+}$* mice. *n* = 3 animals per group; dot-line representing the approximate border
1163 between the periskeletal overgrowth and the bone in the femoral condyle; scale bars, 100
1164 μm. (**E**) Heatmap of LC-MS/MS results showing differentially secreted proteins in
1165 supernatants of *Chmp5^{Ctsk}* relative to *wild-type* skeletal progenitors. *n* = 3 with cells from
1166 3 different animals per group for Nano LC-MS/MS analysis. All data are mean ± s.d., 2-
1167 way ANOVA followed by multiple comparisons or two-tailed unpaired Student's *t*-test for
1168 2-group comparison.
1169
1170 **Fig. S5. Additional x-ray images of *Chmp5^{Ctsk}* mice after treatment with Q + D or the**
1171 **vehicle PEG400 for 7 weeks**. Arrows indicating periskeletal bone overgrowths.
1172
1173 **Fig. S6. CHMP5 is essential for endolysosomal functions and maintaining VPS4A**
1174 **protein in skeletal progenitors.**

1175 (**A**) Representative confocal fluorescence images and quantification of the fluorescence
1176 intensity of LysoTracker Red DND-99 in *Chmp5*^{Ctsk} compared to *wild-type* periskeletal
1177 progenitors. *n* = 11 replicates per group for quantitative analysis; repeated 3 times using
1178 cells from 3 mice. Scale bars, 50 μm. (**B**) Isotype controls for immunofluorescence
1179 staining. Scale bars, 20 μm. (**C**) Co-localization of LAMP1 and RAB7 in *Chmp5*-sufficient
1180 or *Chmp5*-deficient ATDC5 cells. Scale bars, 10 μm. (**D**) Colocalization analysis of
1181 LAMP1 and RAB7 performed by the ImageJ Coloc2 programme and Pearson's R value
1182 (above threshold) shown, *n* = 20 cells per group. (**E**) Representative confocal images of
1183 immunostaining for early endosome marker EEA1, cycling endosome marker RAB11, and
1184 trans-Golgi network marker TGN38 in *Chmp5*^{Ctsk} vs. *wild-type* periskeletal progenitors. *n*
1185 = 30 cells per group. Scale bars, 10 μm (EEA1), 20 μm (RAB11), 25 μm (TGN38). (**F**)
1186 RNA-seq data showing *Vps4a* mRNA expression in *Chmp5*^{Ctsk} vs. *Chmp5*$^{Ctsk/+}$
1187 periskeletal progenitors. *n* = 3 with cells from 3 different animals for each group. (**G**)
1188 Western blot showing that CHMP5 and VPS4A protein expression after transfection of
1189 CHMP5 or empty vector in HEK-293T cells. Experiments repeated 3 times with
1190 independent cells and transfections at different times. (**H**) Quantitative PCR showing the
1191 expression of *CHMP5* and *VPS4A* mRNA after transfecting CHMP5 or empty vector in
1192 HEK-293T cells. *n* = 3 replicates for each group, experiments repeated 3 times with
1193 independent cells and transfections at different times. All data shown as mean ± s.d.; two-
1194 tailed unpaired Student's *t*-test.
1195
1196 **Fig. S7. Mitochondrial dysfunction and activation of DNA damage-induced**
1197 **senescence in *Chmp5*-deficient skeletal progenitors.**

1198 (**A**) Representative TMRE confocal images showing accumulation of mitochondria in
1199 *Chmp5*^{Ctsk} periskeletal progenitors. *n* = 30 cells per group, scale bars, 25 μm. (**B**)
1200 Confocal fluorescence imaging mapping intracellular ROS (CellROX Deep Red) and
1201 mitochondria (MitoTracker Green) in ATDC5 cells with or without *Chmp5* depletion. *n* =
1202 20 cells for each group; scale bars, 10 μm. The right histogram showing the quantification
1203 of CellROX Deep Red in ATDC5 cells by flow cytometry. *n* = 3 per group, experiment
1204 repeated twice. (**C**) GSEA of RNA-seq data showing positive enrichment of genes
1205 associated with the molecular pathway of DNA damage-induced senescence in
1206 *Chmp5*^{Ctsk} relative to *Chmp5*$^{Ctsk/+}$ periskeletal progenitors. (**D**) Quantitative PCR
1207 determining expression of *H2afx* and *Trp53* genes in *Chmp5*^{Ctsk} relative to *Chmp5*$^{Ctsk/+}$
1208 periskeletal progenitors. *n* = 6 with cells from different animals per group. Data shown as
1209 mean ± s.d.; two-tailed unpaired Student's *t*-test.

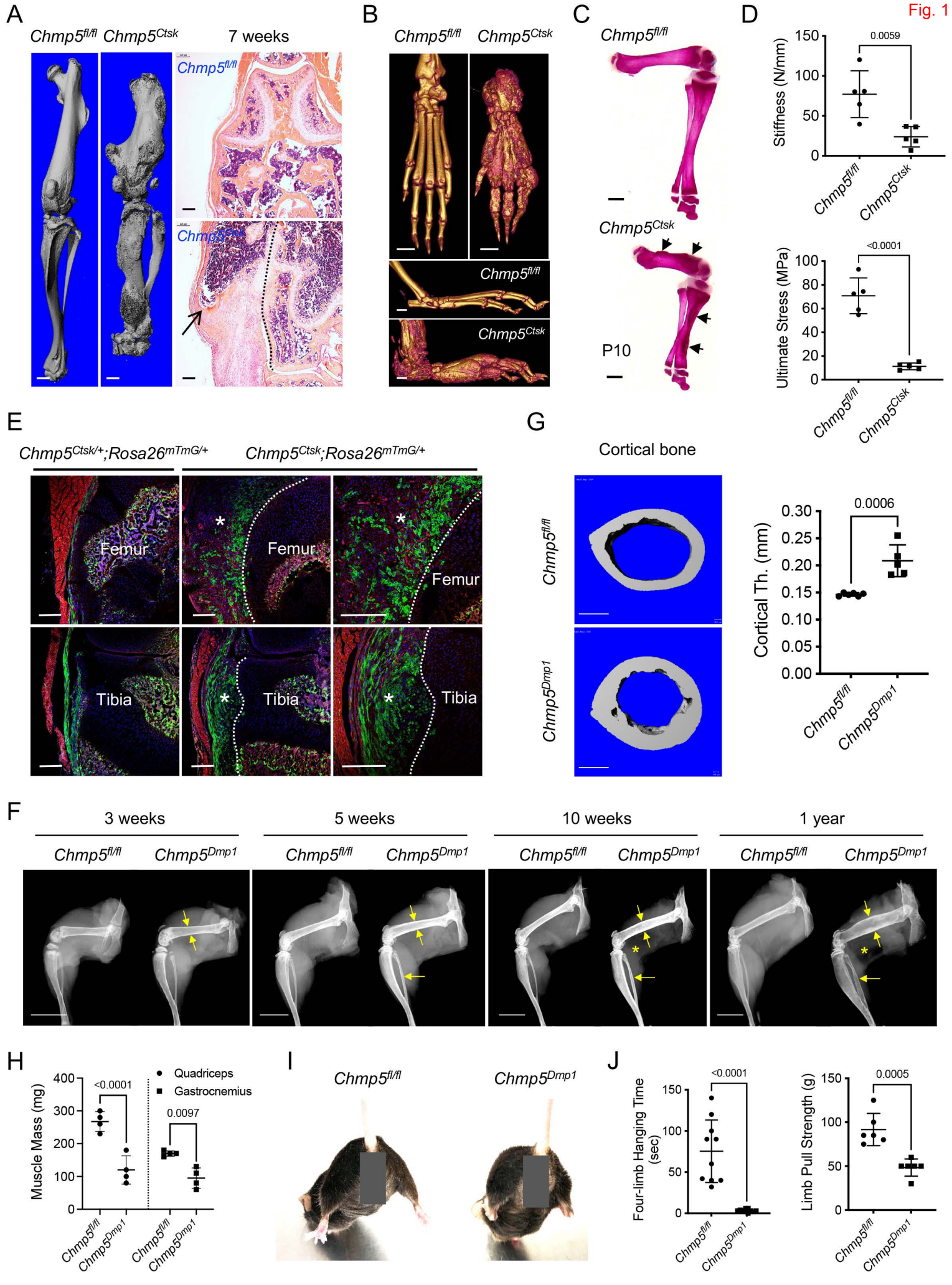
A
Chmp5fl/fl Chmp5Ctsk
7 weeks
Chmp5fl/fl
Chmp5Ctsk
B
Chmp5fl/fl Chmp5Ctsk
Chmp5fl/fl
Chmp5Ctsk
C
Chmp5fl/fl
Chmp5Ctsk
P10
D
Stiffness (N/mm)
0.0059
Chmp5fl/fl
Chmp5Ctsk
Ultimate Stress (MPa)
<0.0001
Chmp5fl/fl
Chmp5Ctsk
E
Chmp5Ctsk/+;Rosa26mTmG/+
Chmp5Ctsk;Rosa26mTmG/+
Femur
Tibia
G
Cortical bone
Chmp5fl/fl
Chmp5Dmp1
Cortical Th. (mm)
0.0006
Chmp5fl/fl
Chmp5Dmp1
F
3 weeks
5 weeks
10 weeks
1 year
Chmp5fl/fl
Chmp5Dmp1
H
Muscle Mass (mg)
Quadriceps
Gastrocnemius
<0.0001
0.0097
Chmp5fl/fl
Chmp5Dmp1
I
Chmp5fl/fl
Chmp5Dmp1
J
Four-limb Hanging Time (sec)
<0.0001
Chmp5fl/fl
Chmp5Dmp1
Limb Pull Strength (g)
0.0005
Chmp5fl/fl
Chmp5Dmp1

A

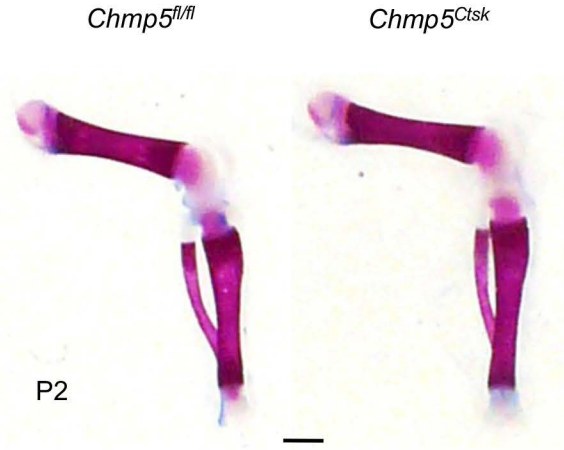
Chmp5fl/fl
Chmp5Ctsk
P2

B

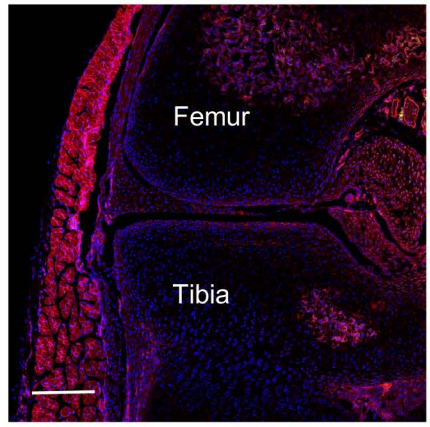
Cre negative control
Femur
Tibia

C

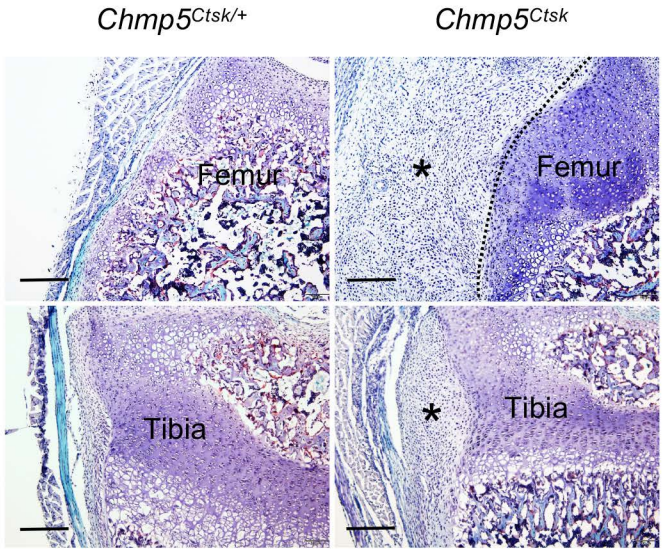
Chmp5Ctsk/+
Chmp5Ctsk
Femur
Femur
*
Tibia
Tibia
*

D

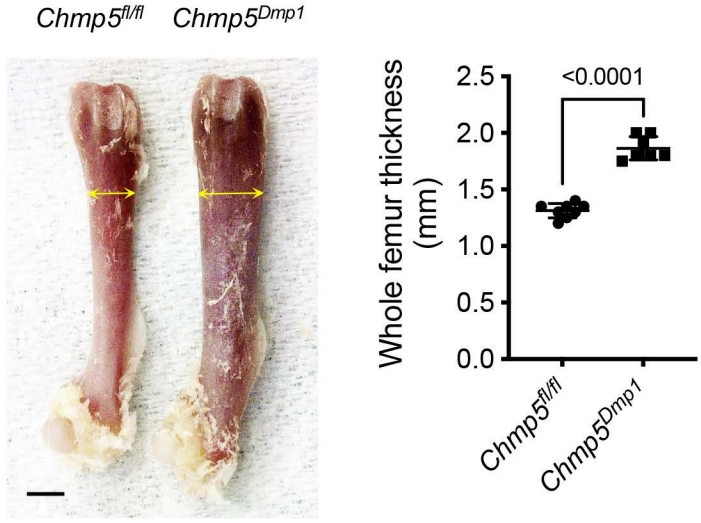
Chmp5fl/fl
Chmp5Dmp1
Whole femur thickness (mm)
2.5
2.0
1.5
1.0
0.5
0.0
<0.0001
Chmp5fl/fl
Chmp5Dmp1

E

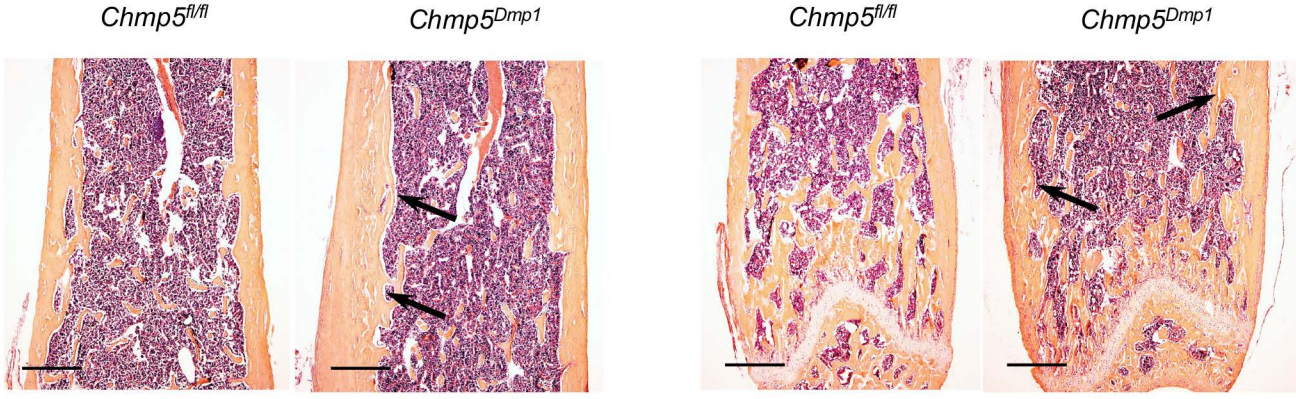
Chmp5fl/fl
Chmp5Dmp1
Chmp5fl/fl
Chmp5Dmp1

A

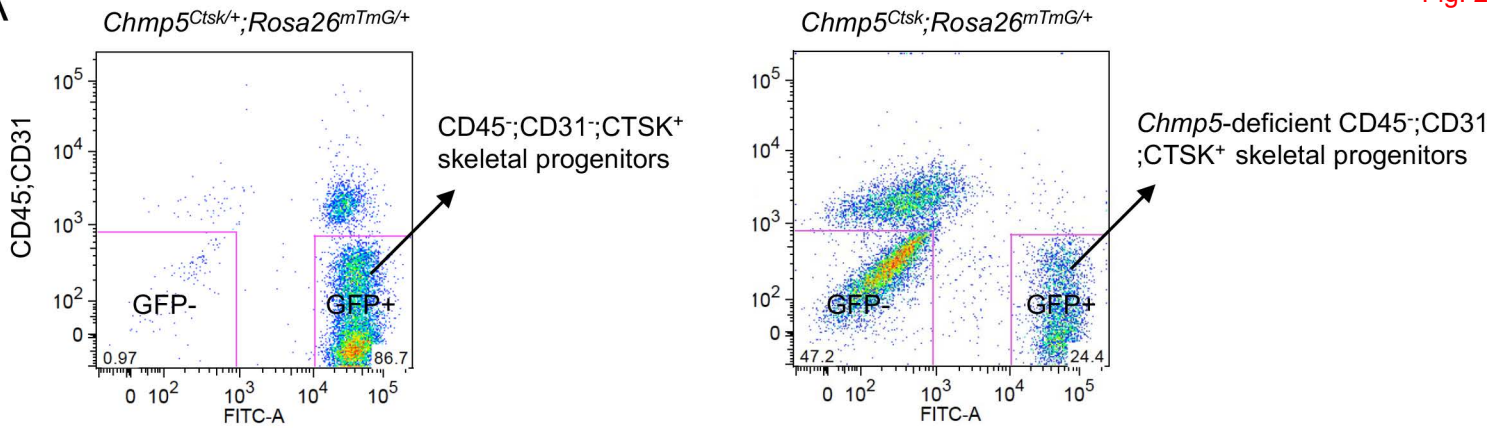

B

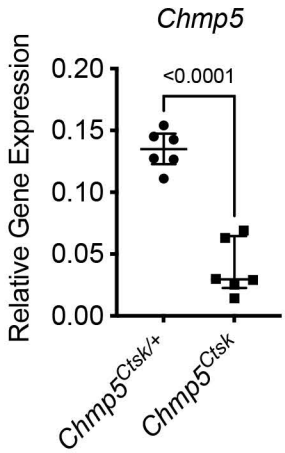

C

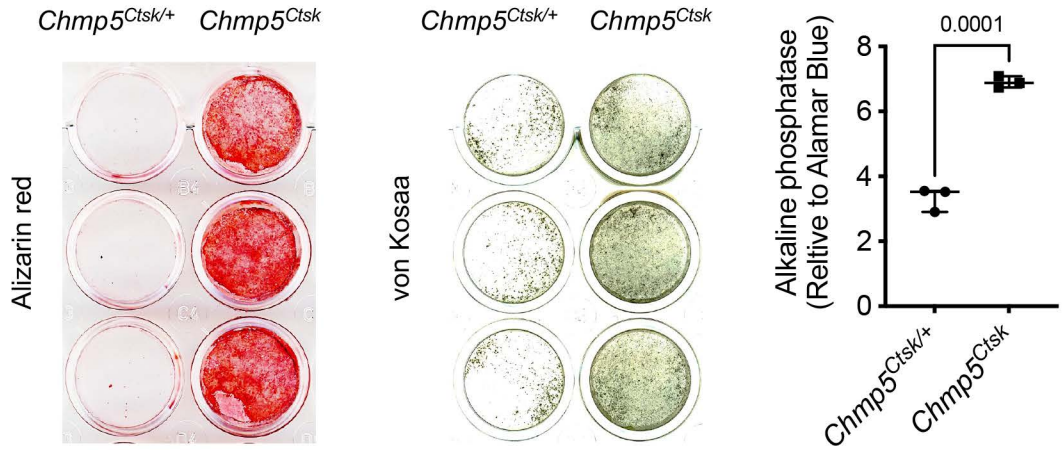

D

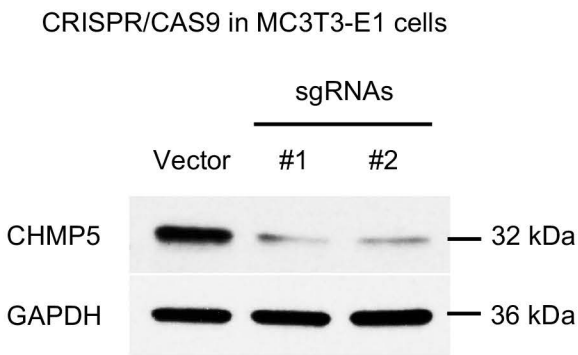

E

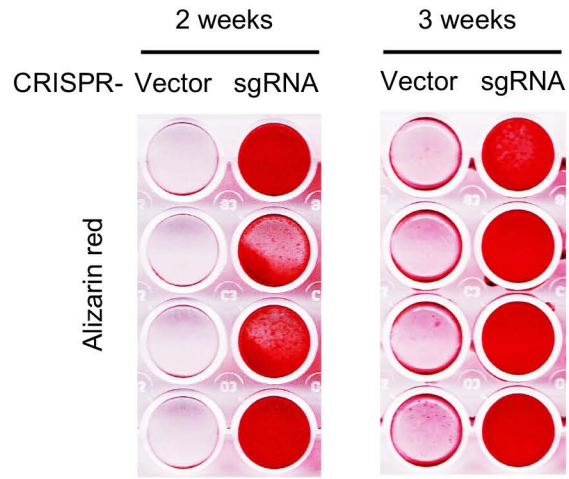

F

Ingenuity pathway analysis of RNA-seq data (*Chmp5*^{Ctsk} vs. *Chmp5*$^{Ctsk/+}$)

Diseases or Functions Annotation	p-Value	Predicted Activation State	Activation z-score	# Molecules
Differentiation of osteoblastic-lineage cells	0.00000101	**Increased**	2.365	44
Differentiation of bone	6.05E-11	**Increased**	2.229	71
Differentiation of osteoblasts	0.00000197	**Increased**	2.101	43
Differentiation of bone cells	1.05E-10	**Increased**	2.1	70

A

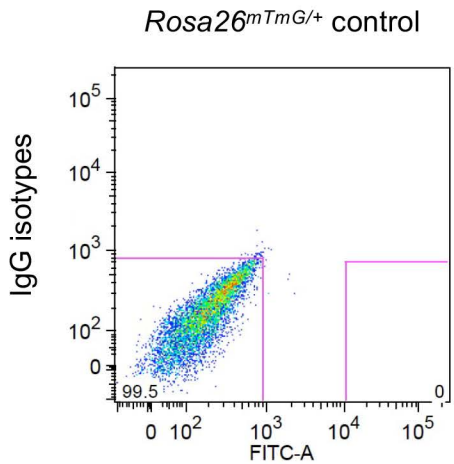
Rosa26mTmG/+ control
IgG isotypes
FITC-A
99.5
0

B

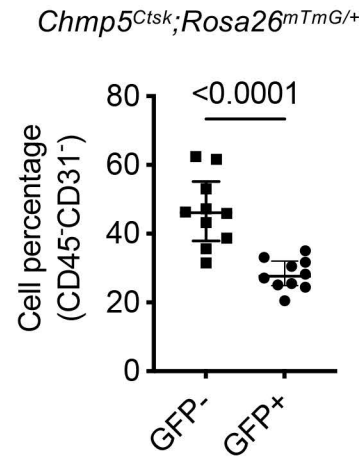
Chmp5Ctsk;Rosa26mTmG/+
<0.0001
Cell percentage (CD45-CD31-)
GFP-
GFP+

A

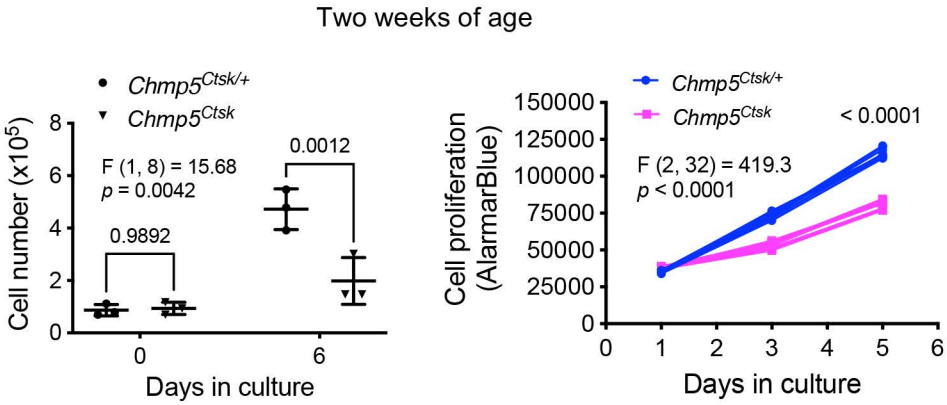
Two weeks of age
Chmp5Ctsk/+
Chmp5Ctsk
Cell number (x10^5)
F (1, 8) = 15.68
p = 0.0042
0.0012
0.9892
Days in culture
Cell proliferation (AlarmarBlue)
F (2, 32) = 419.3
p < 0.0001
< 0.0001
Days in culture

B

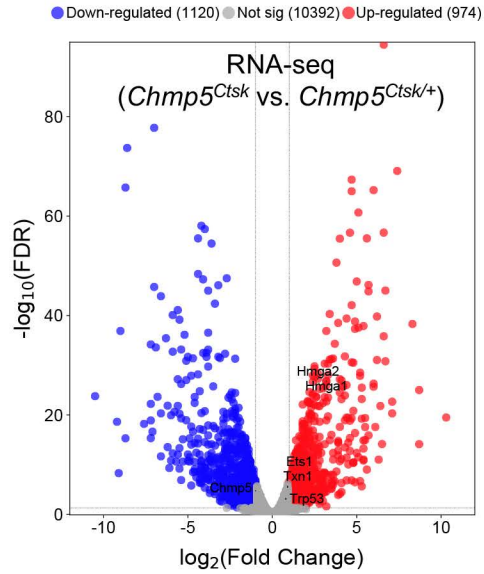
Down-regulated (1120)
Not sig (10392)
Up-regulated (974)
RNA-seq
(Chmp5Ctsk vs. Chmp5Ctsk/+)
-log10(FDR)
log2(Fold Change)
Hmga2
Hmga1
Ets1
Txn1
Trp53
Chmp5

C

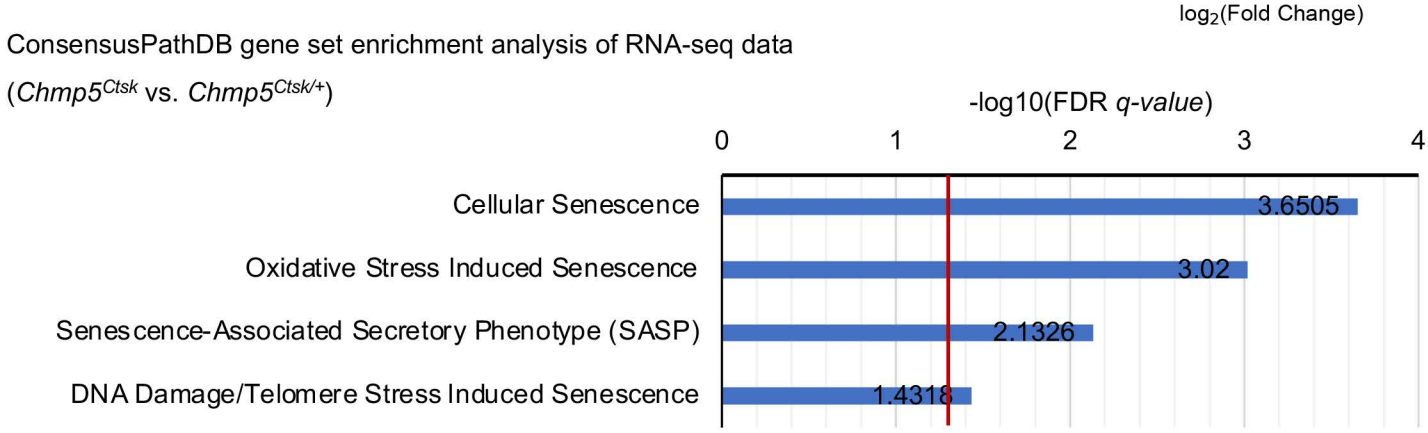
ConsensusPathDB gene set enrichment analysis of RNA-seq data
(Chmp5Ctsk vs. Chmp5Ctsk/+)
-log10(FDR q-value)
Cellular Senescence
3.6505
Oxidative Stress Induced Senescence
3.02
Senescence-Associated Secretory Phenotype (SASP)
2.1326
DNA Damage/Telomere Stress Induced Senescence
1.4318

D

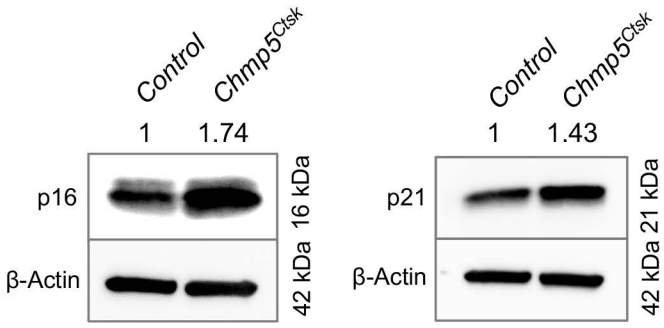
Control
Chmp5Ctsk
1
1.74
p16
β-Actin
16 kDa
42 kDa
1
1.43
p21
β-Actin
21 kDa
42 kDa

E

Chmp5Ctsk/+
Chmp5Ctsk

F

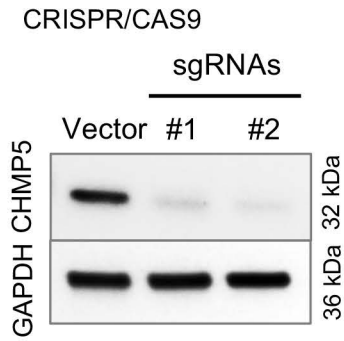
CRISPR/CAS9
sgRNAs
Vector
#1
#2
CHMP5
GAPDH
32 kDa
36 kDa

G

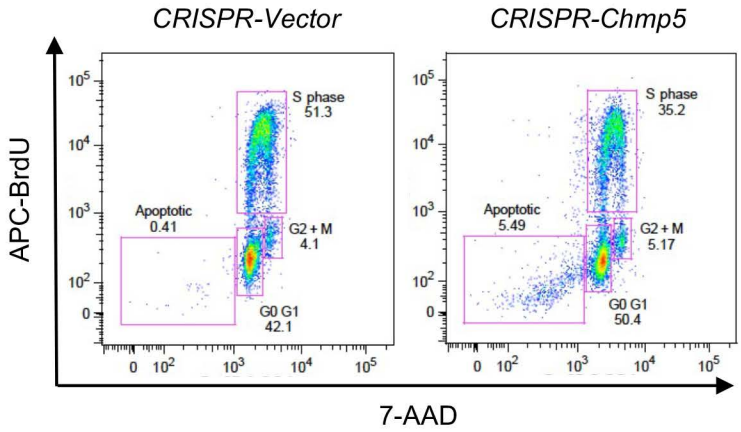
CRISPR-Vector
CRISPR-Chmp5
APC-BrdU
7-AAD
S phase
51.3
Apoptotic
0.41
G2 + M
4.1
G0 G1
42.1
S phase
35.2
Apoptotic
5.49
G2 + M
5.17
G0 G1
50.4

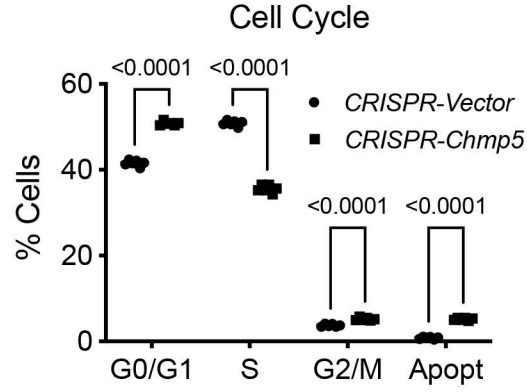
Cell Cycle
% Cells
<0.0001
<0.0001
<0.0001
<0.0001
CRISPR-Vector
CRISPR-Chmp5
G0/G1
S
G2/M
Apopt

A

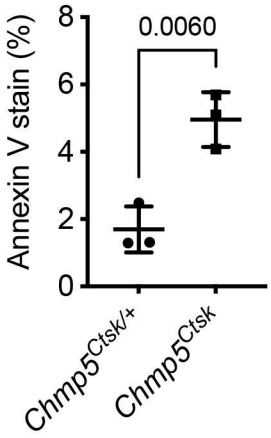
Annexin V stain (%)
0.0060
Chmp5Ctsk/+
Chmp5Ctsk

B

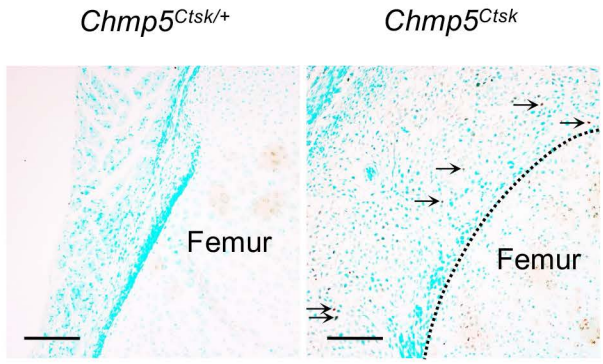
Chmp5Ctsk/+
Chmp5Ctsk
Femur
Femur

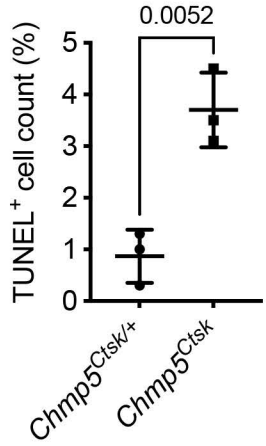
TUNEL+ cell count (%)
0.0052
Chmp5Ctsk/+
Chmp5Ctsk

C

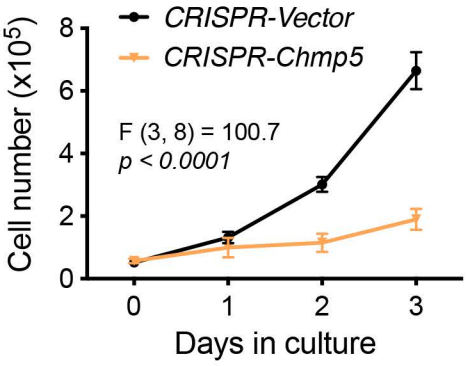
CRISPR-Vector
CRISPR-Chmp5
F (3, 8) = 100.7
p < 0.0001
Cell number (x10^5)
Days in culture

D

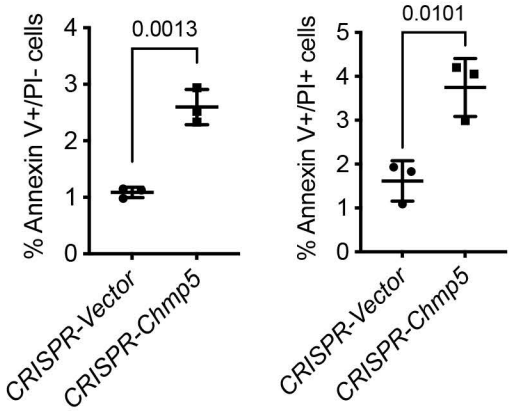
% Annexin V+/PI- cells
0.0013
CRISPR-Vector
CRISPR-Chmp5
% Annexin V+/PI+ cells
0.0101
CRISPR-Vector
CRISPR-Chmp5

E

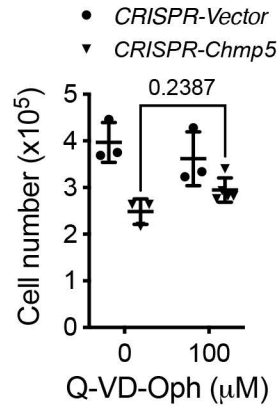
CRISPR-Vector
CRISPR-Chmp5
Cell number (x10^5)
0.2387
Q-VD-Oph (μM)

A

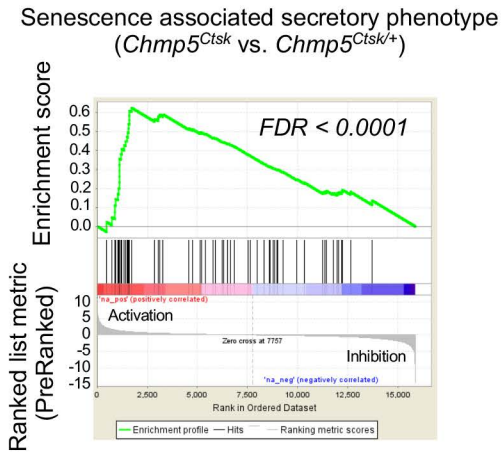
Senescence associated secretory phenotype
(Chmp5Ctsk vs. Chmp5Ctsk/+)
Enrichment score
FDR < 0.0001
Ranked list metric
(PreRanked)
Activation
Inhibition
Rank in Ordered Dataset
Enrichment profile
Hits
Ranking metric scores

B

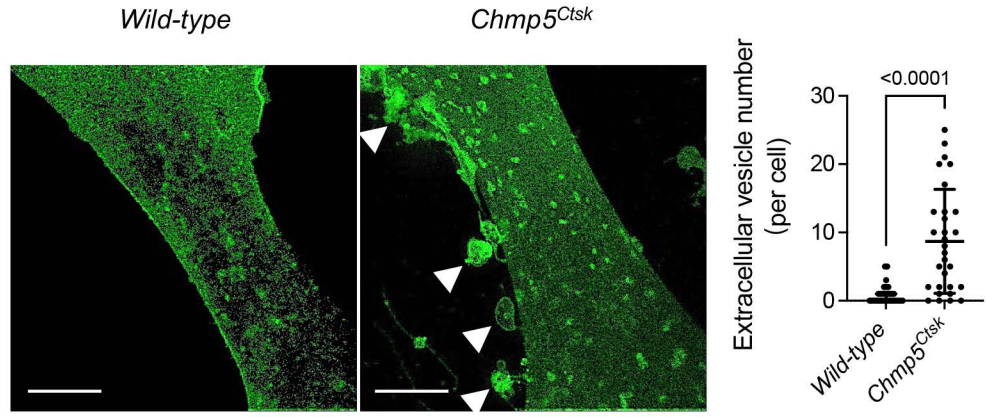
Wild-type
Chmp5Ctsk
Extracellular vesicle number
(per cell)
<0.0001
Wild-type
Chmp5Ctsk

C

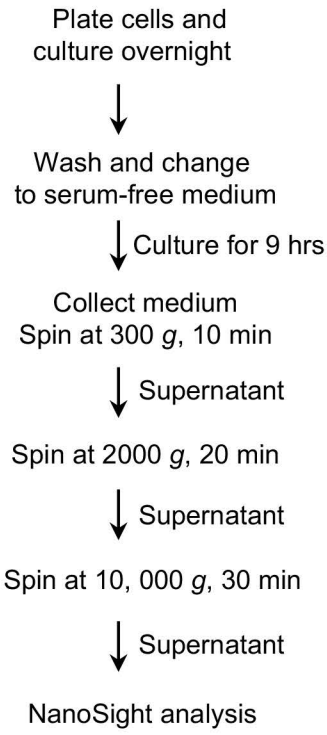
Plate cells and
culture overnight
Wash and change
to serum-free medium
Culture for 9 hrs
Collect medium
Spin at 300 g, 10 min
Supernatant
Spin at 2000 g, 20 min
Supernatant
Spin at 10, 000 g, 30 min
Supernatant
NanoSight analysis

D

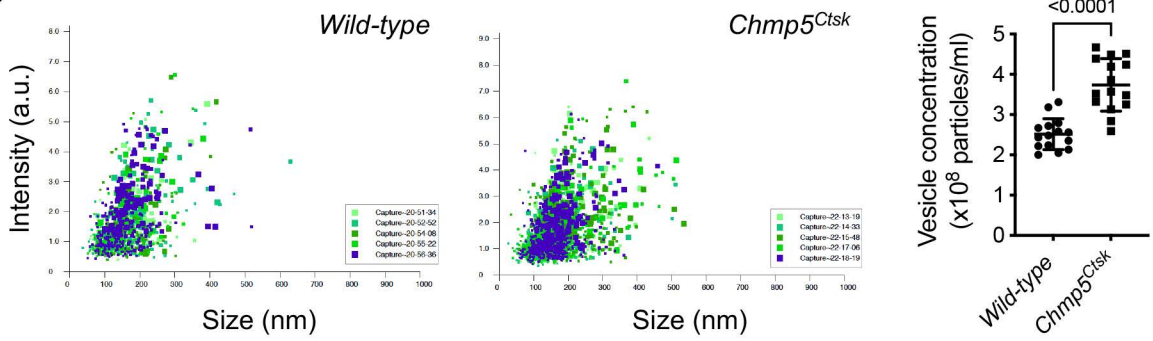
Wild-type
Chmp5Ctsk
Intensity (a.u.)
Size (nm)
Size (nm)
Vesicle concentration
(x10^8 particles/ml)
<0.0001
Wild-type
Chmp5Ctsk

E

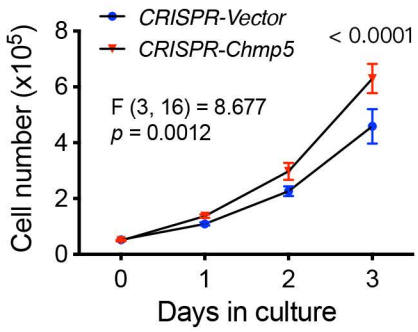
CRISPR-Vector
CRISPR-Chmp5
< 0.0001
F (3, 16) = 8.677
p = 0.0012
Cell number (x10^5)
Days in culture

F

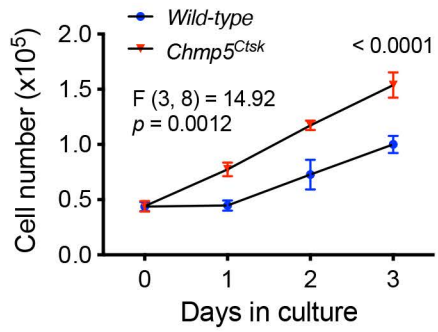
Wild-type
Chmp5Ctsk
< 0.0001
F (3, 8) = 14.92
p = 0.0012
Cell number (x10^5)
Days in culture

G

2 weeks
Wild-type
Chmp5Ctsk
CD45-CD31-GFP- cells

H

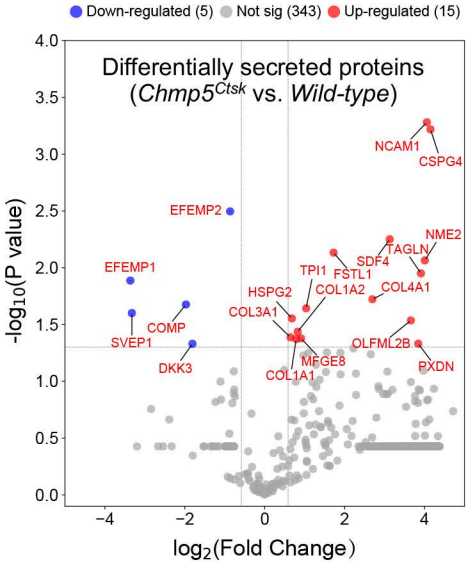
Down-regulated (5)
Not sig (343)
Up-regulated (15)
Differentially secreted proteins
(Chmp5Ctsk vs. Wild-type)
NCAM1
CSPG4
EFEMP2
NME2
TAGLN
SDF4
TPI1
FSTL1
EFEMP1
HSPG2
COL1A2
COL4A1
COL3A1
COMP
SVEP1
OLFML2B
DKK3
MFGE8
PXDN
COL1A1
-log10(P value)
log2(Fold Change)

I

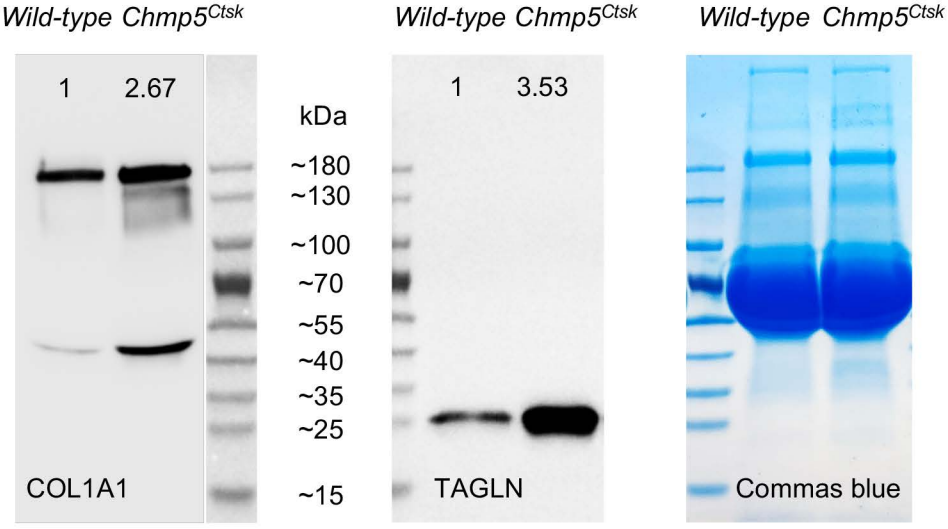
Wild-type
Chmp5Ctsk
1
2.67
kDa
~180
~130
~100
~70
~55
~40
~35
~25
~15
COL1A1
Wild-type
Chmp5Ctsk
1
3.53
TAGLN
Wild-type
Chmp5Ctsk
Commas blue

A

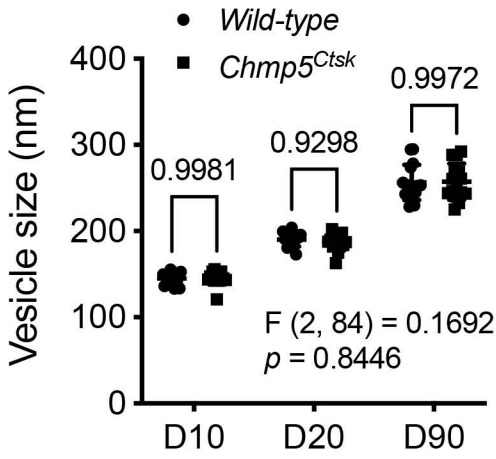

B

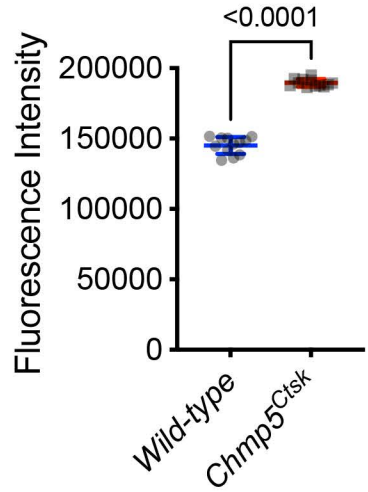

C

D

Ki-67 immunostaining

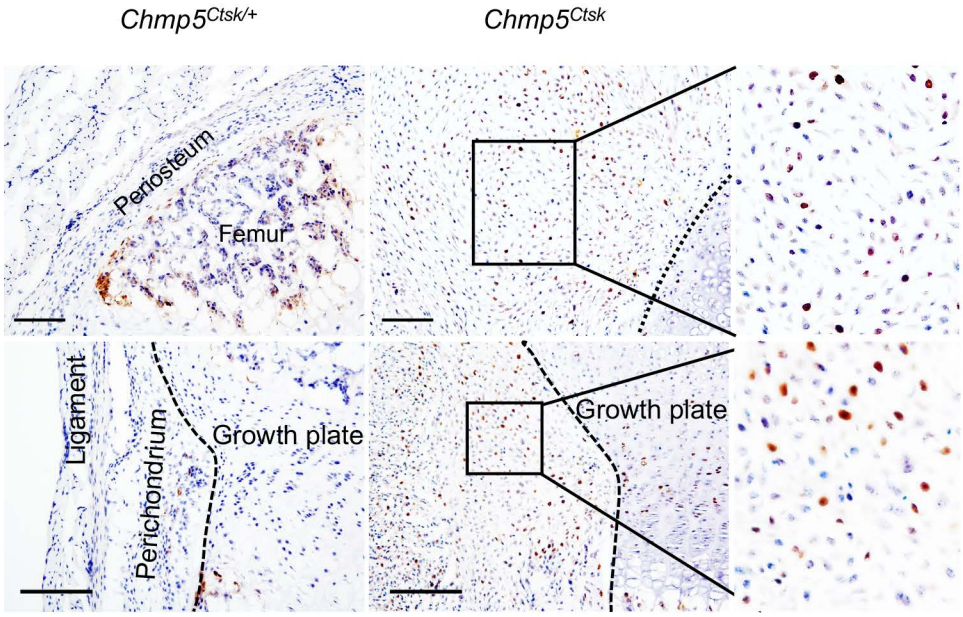

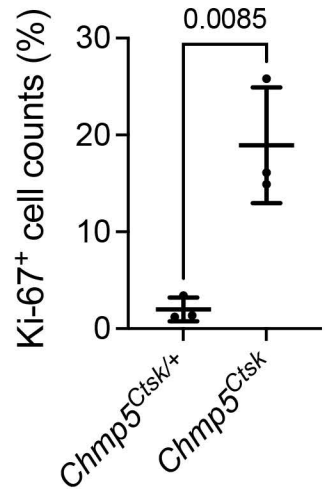

E

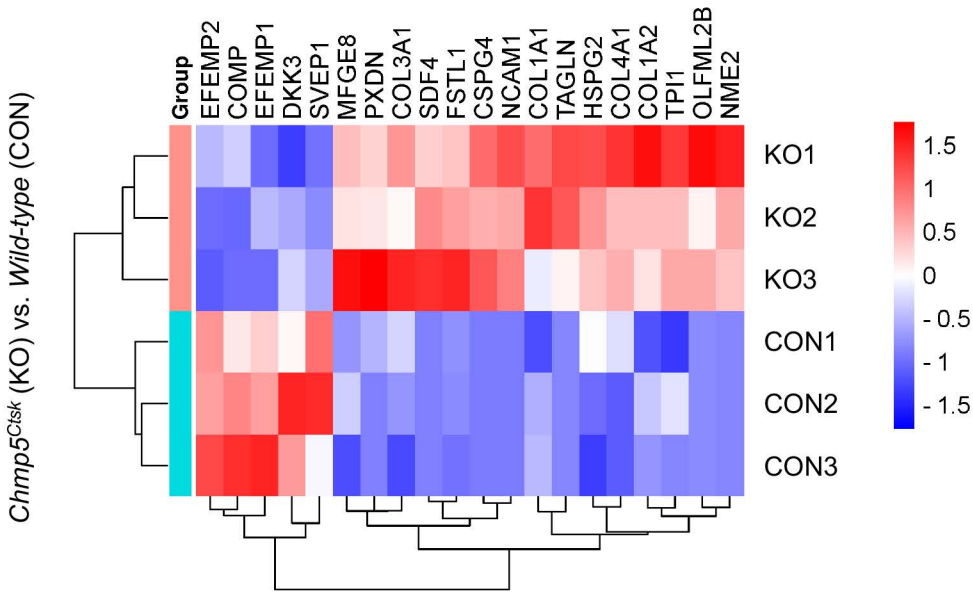

A

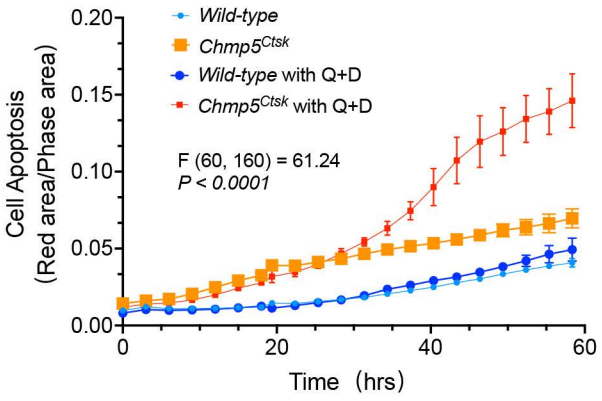
Wild-type
Chmp5Ctsk
Wild-type with Q+D
Chmp5Ctsk with Q+D
F (60, 160) = 61.24
P < 0.0001
Cell Apoptosis
(Red area/Phase area)
0.20
0.15
0.10
0.05
0.00
0
20
40
60
Time (hrs)

C

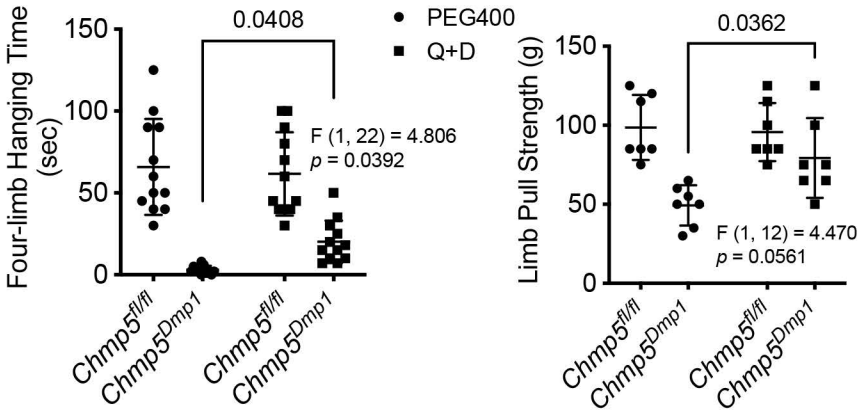
Four-limb Hanging Time
(sec)
150
100
50
0
0.0408
PEG400
Q+D
F (1, 22) = 4.806
p = 0.0392
Chmp5fl/fl
Chmp5Dmp1
Chmp5fl/fl
Chmp5Dmp1
Limb Pull Strength (g)
150
100
50
0
0.0362
F (1, 12) = 4.470
p = 0.0561
Chmp5fl/fl
Chmp5Dmp1
Chmp5fl/fl
Chmp5Dmp1

B

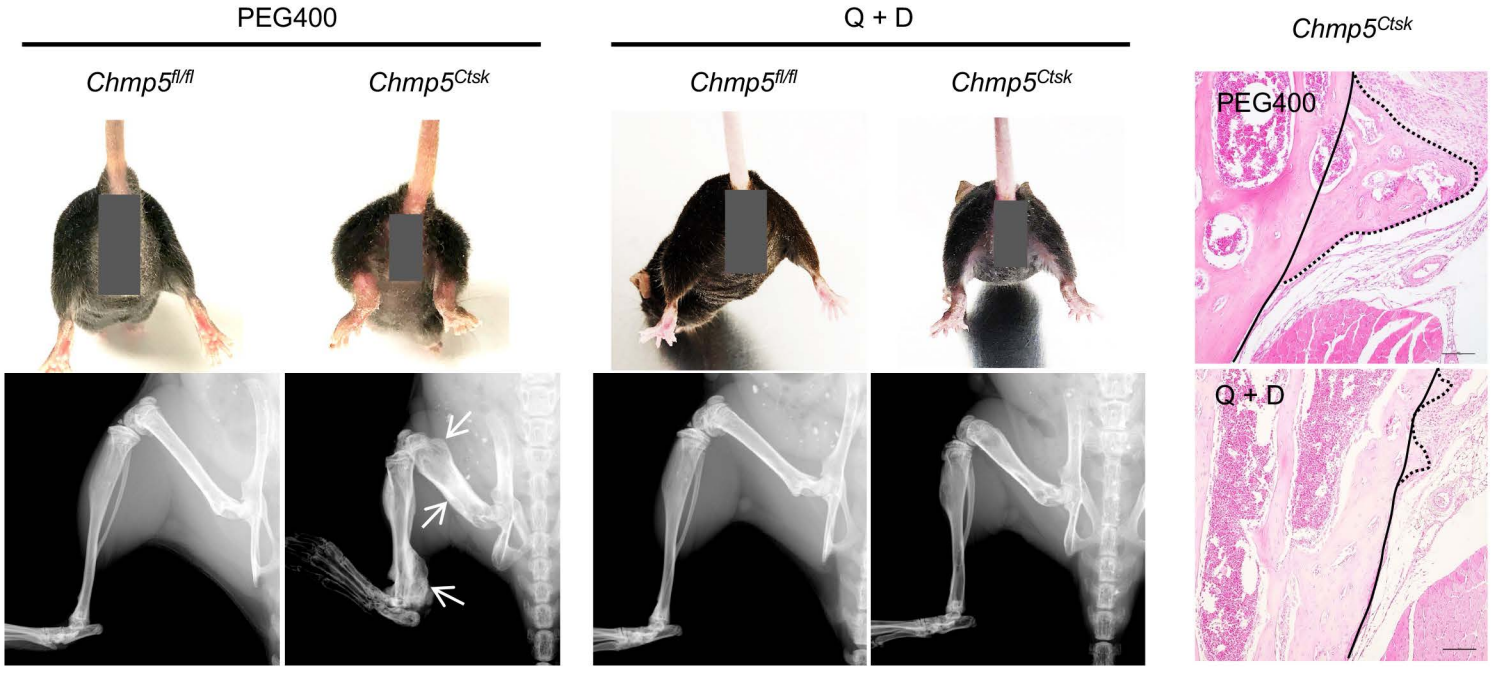
PEG400
Q + D
Chmp5fl/fl
Chmp5Ctsk
Chmp5fl/fl
Chmp5Ctsk
Chmp5Ctsk
PEG400
Q + D

D

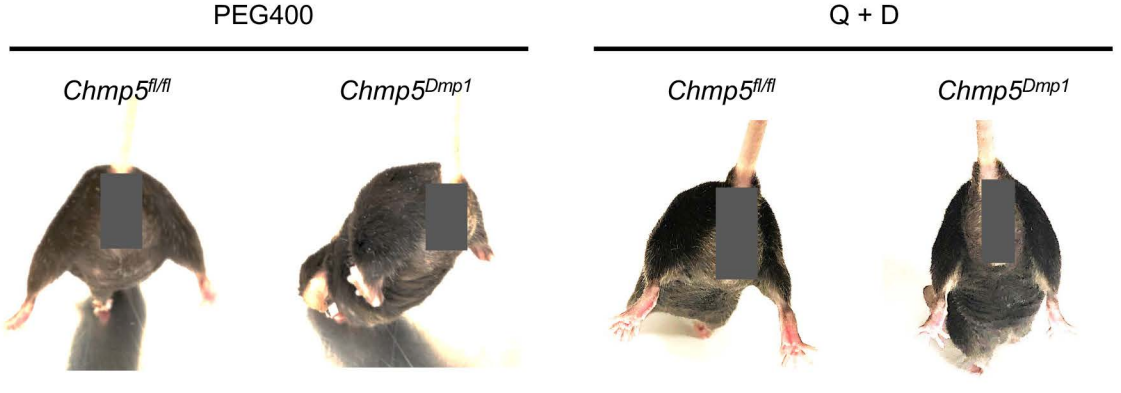
PEG400
Q + D
Chmp5fl/fl
Chmp5Dmp1
Chmp5fl/fl
Chmp5Dmp1

E

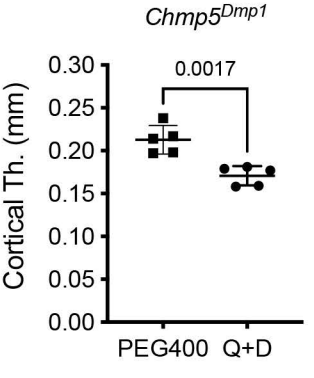
Chmp5Dmp1
Cortical Th. (mm)
0.30
0.25
0.20
0.15
0.10
0.05
0.00
0.0017
PEG400
Q+D

Fig. S5

Chmp5^{Ctsk}

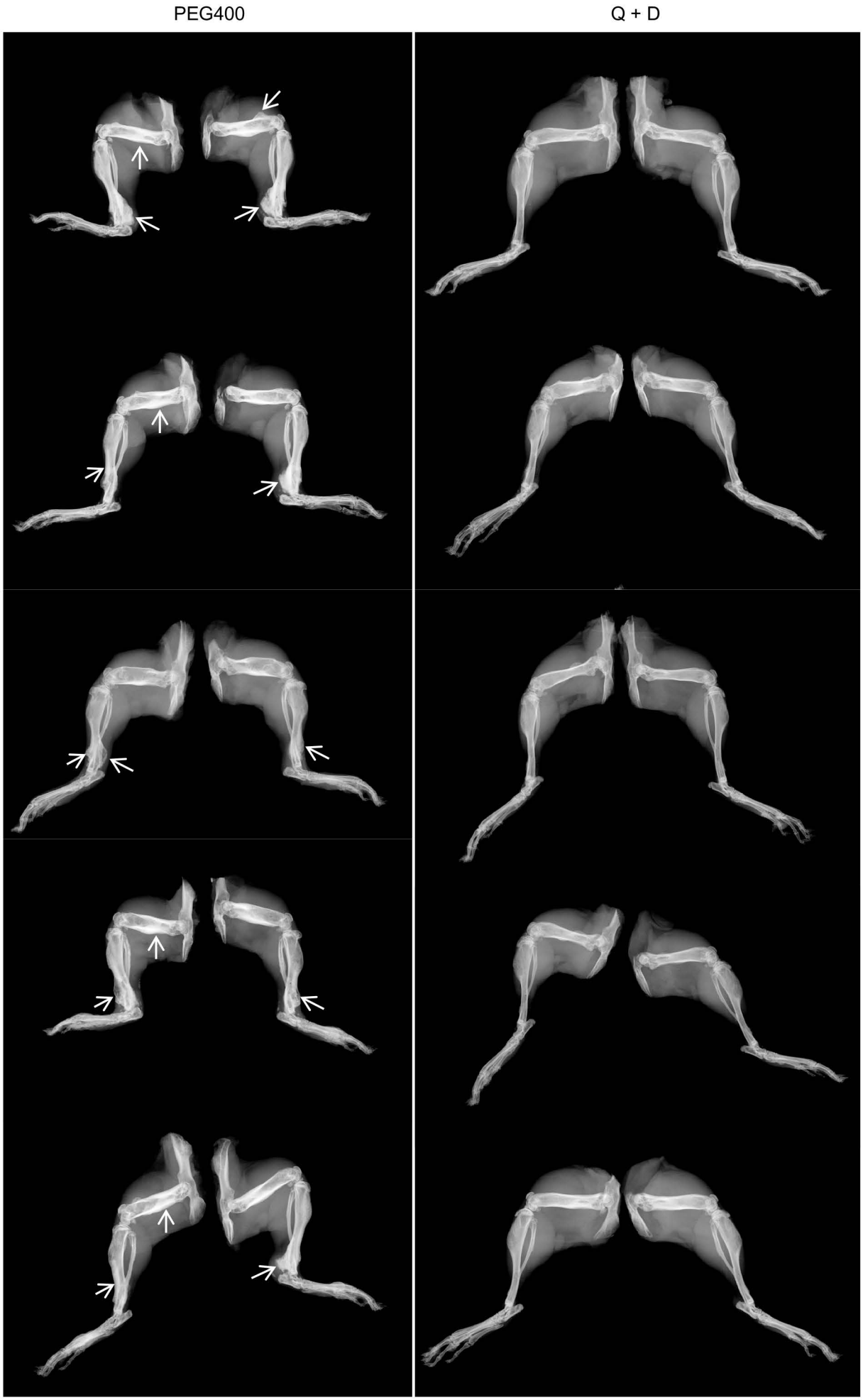

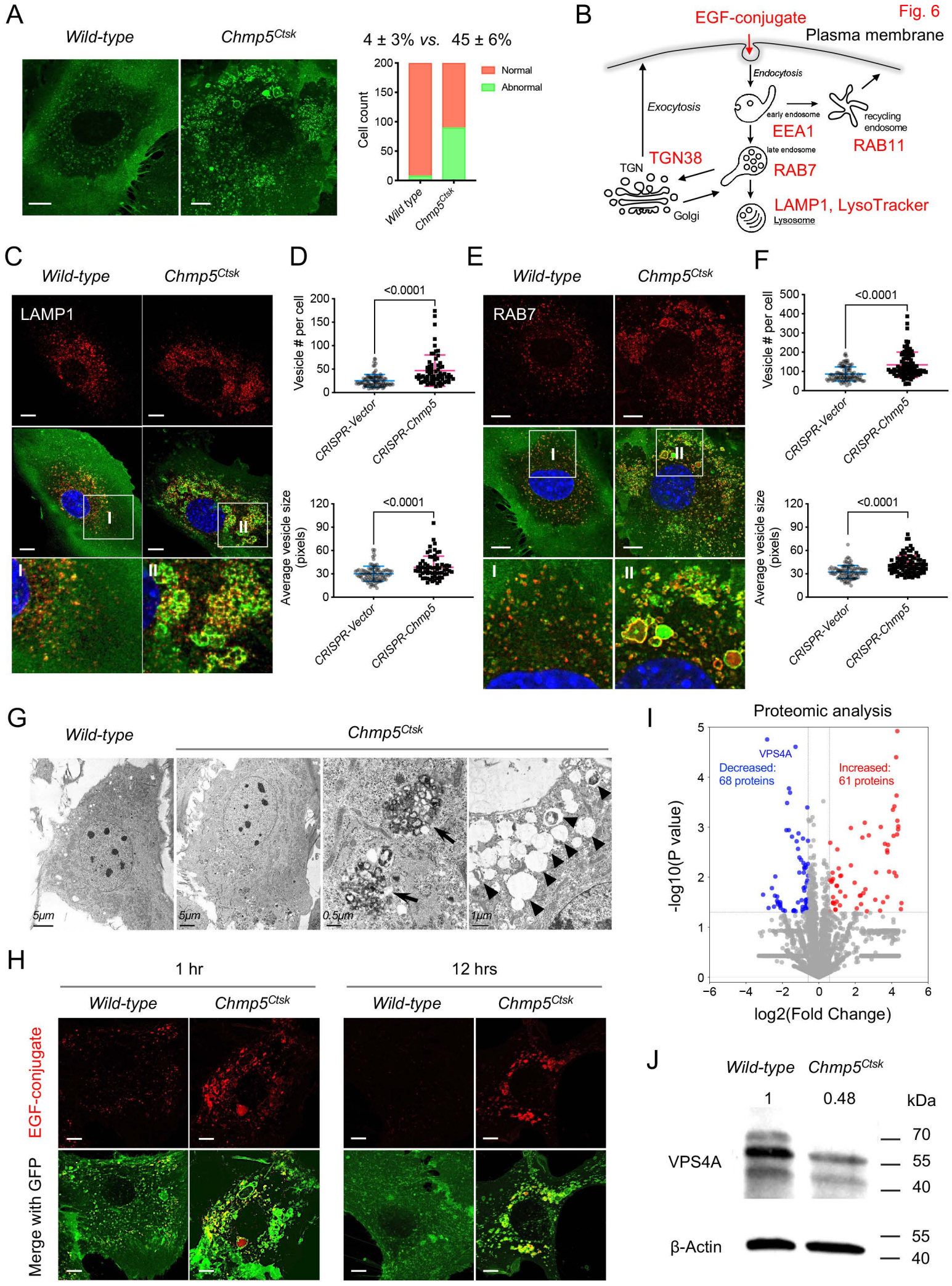
Fig. 6
A
Wild-type
Chmp5Ctsk
4 ± 3% vs. 45 ± 6%
Cell count
Normal
Abnormal
Wild type
Chmp5Ctsk
B
EGF-conjugate
Plasma membrane
Endocytosis
Exocytosis
early endosome
recycling endosome
EEA1
RAB11
late endosome
TGN38
TGN
RAB7
Golgi
LAMP1, LysoTracker
Lysosome
C
Wild-type
Chmp5Ctsk
LAMP1
D
Vesicle # per cell
<0.0001
CRISPR-Vector
CRISPR-Chmp5
Average vesicle size (pixels)
E
RAB7
F
G
Wild-type
Chmp5Ctsk
5μm
0.5μm
1μm
H
1 hr
12 hrs
EGF-conjugate
Merge with GFP
I
Proteomic analysis
VPS4A
Decreased: 68 proteins
Increased: 61 proteins
-log10(P value)
log2(Fold Change)
J
Wild-type
Chmp5Ctsk
1
0.48
kDa
VPS4A
β-Actin
70
55
40

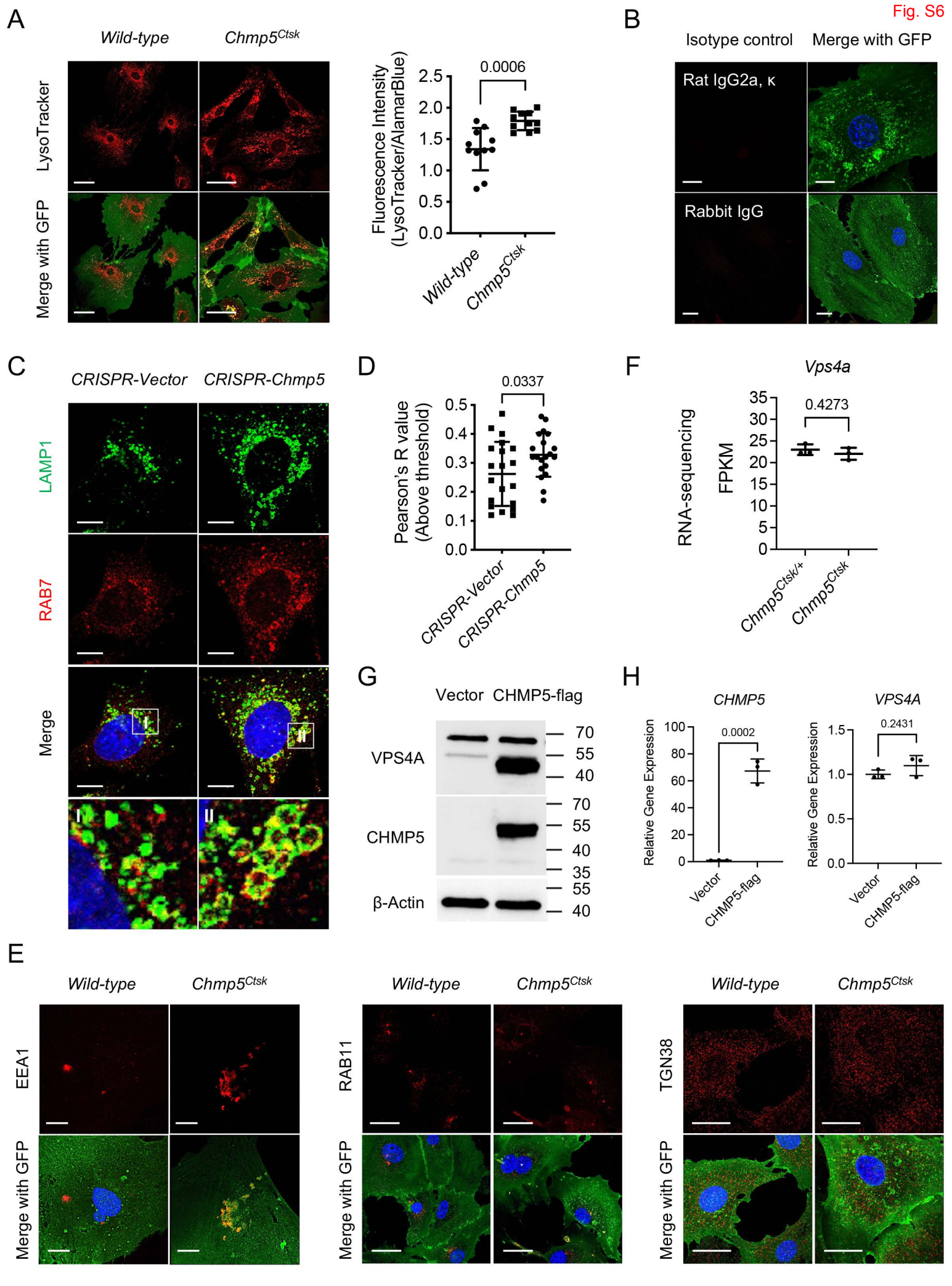
A
Wild-type
Chmp5Ctsk
LysoTracker
Merge with GFP
Fluorescence Intensity (LysoTracker/AlamarBlue)
0.0006
2.5
2.0
1.5
1.0
0.5
0.0
Wild-type
Chmp5Ctsk
B
Isotype control
Merge with GFP
Rat IgG2a, κ
Rabbit IgG
C
CRISPR-Vector
CRISPR-Chmp5
LAMP1
RAB7
Merge
I
II
D
Pearson's R value (Above threshold)
0.0337
0.5
0.4
0.3
0.2
0.1
0.0
CRISPR-Vector
CRISPR-Chmp5
F
Vps4a
RNA-sequencing
FPKM
0.4273
35
30
25
20
15
10
5
0
Chmp5Ctsk/+
Chmp5Ctsk
G
Vector
CHMP5-flag
VPS4A
CHMP5
β-Actin
70
55
40
70
55
40
35
55
40
H
CHMP5
VPS4A
Relative Gene Expression
0.0002
0.2431
100
80
60
40
20
0
1.5
1.0
0.5
0.0
Vector
CHMP5-flag
E
Wild-type
Chmp5Ctsk
EEA1
RAB11
TGN38
Merge with GFP

A

Oxidative stress-induced senescence
(*Chmp5*^{Ctsk} vs. *Chmp5*$^{Ctsk/+}$)

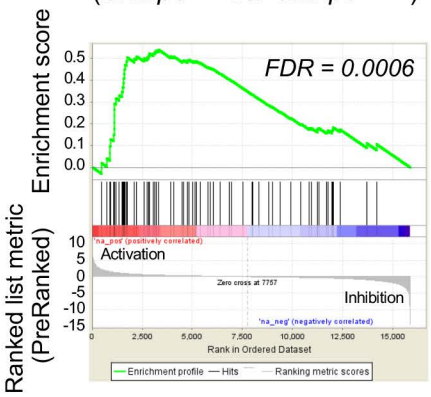

B

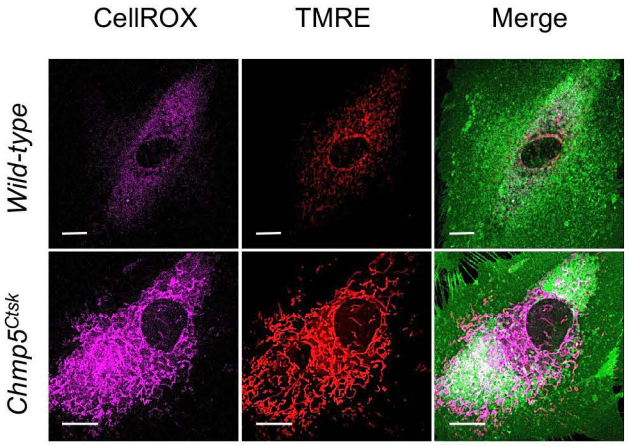

Celluar Oxidative Stress

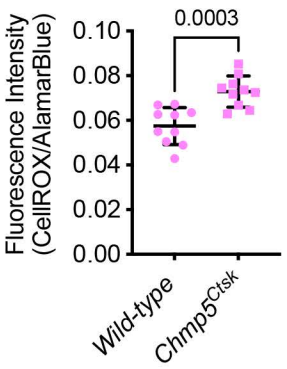

C

TMRE fluorescence intensity

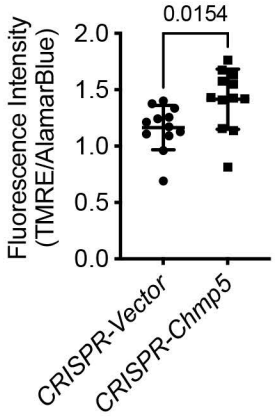

D

CRISPR-vector gRNA

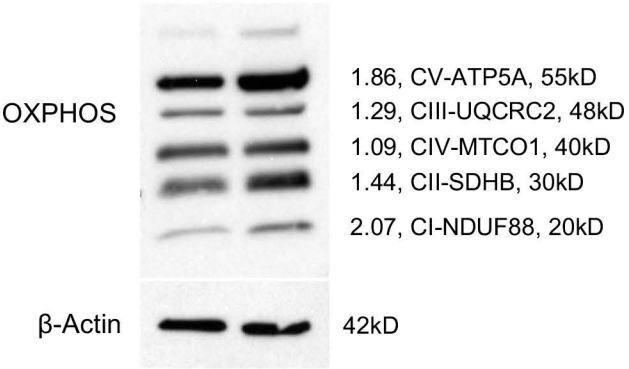

E

Galactose medium

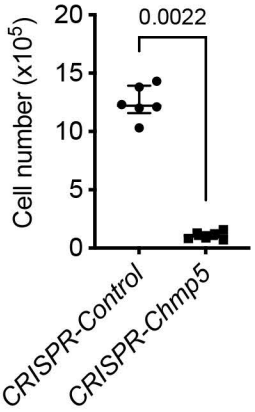

F

Spare respiratory capacity

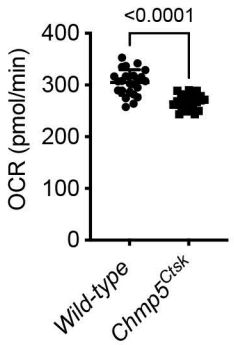

Extracellular acidification rate

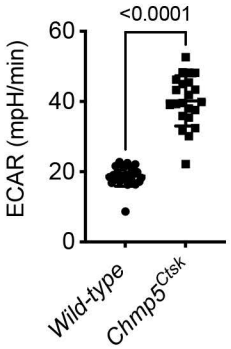

G

• *CRISPR-Vector* ▾ *CRISPR-Chmp5*

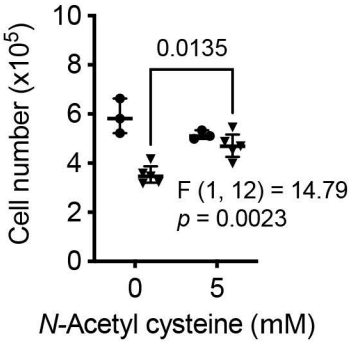

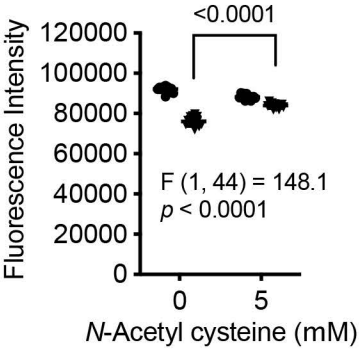

H

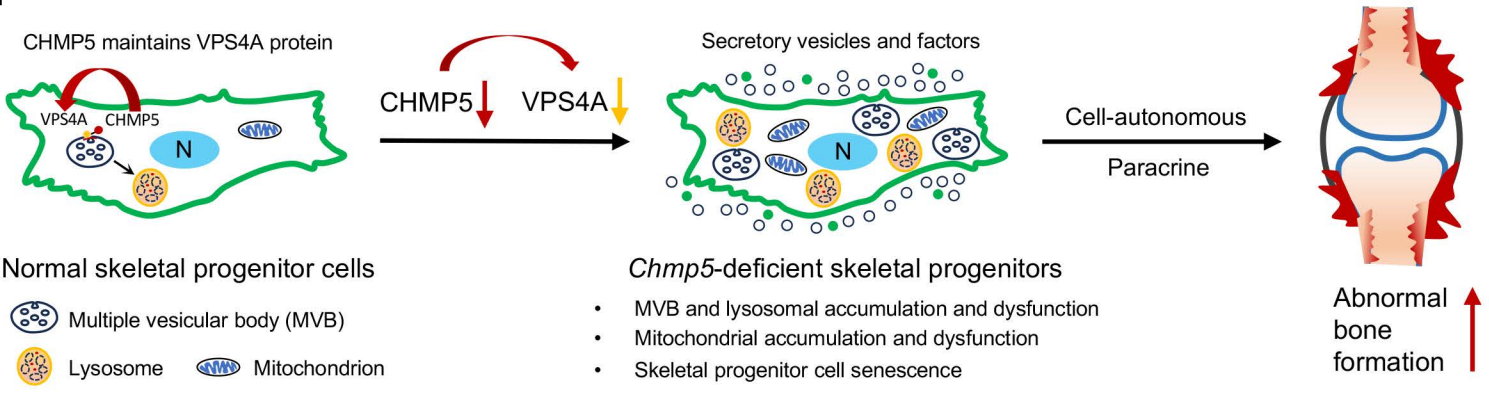

A

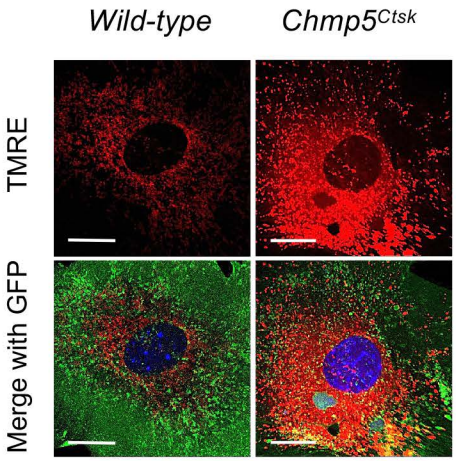
Wild-type
Chmp5Ctsk
TMRE
Merge with GFP

B

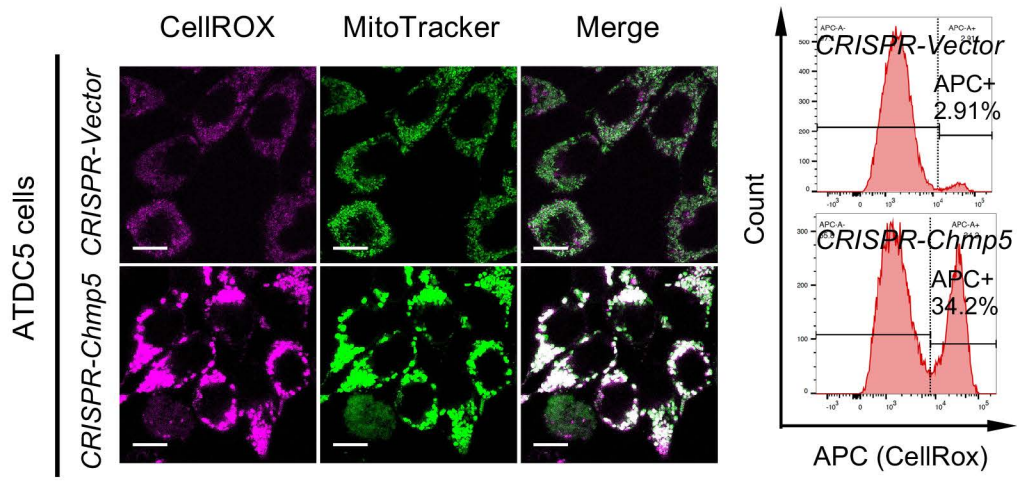
CellROX
MitoTracker
Merge
ATDC5 cells
CRISPR-Vector
CRISPR-Chmp5
CRISPR-Vector
APC+
2.91%
CRISPR-Chmp5
APC+
34.2%
Count
APC (CellRox)

C

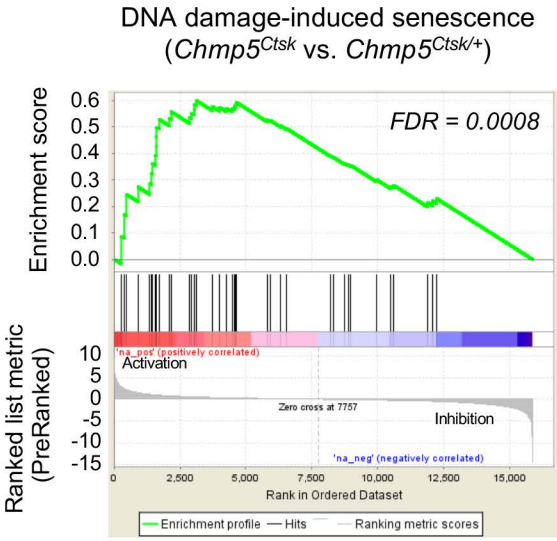
DNA damage-induced senescence
(Chmp5Ctsk vs. Chmp5Ctsk/+)
FDR = 0.0008
Enrichment score
Ranked list metric
(PreRanked)
Activation
Inhibition
Zero cross at 7757
Rank in Ordered Dataset
Enrichment profile
Hits
Ranking metric scores

D

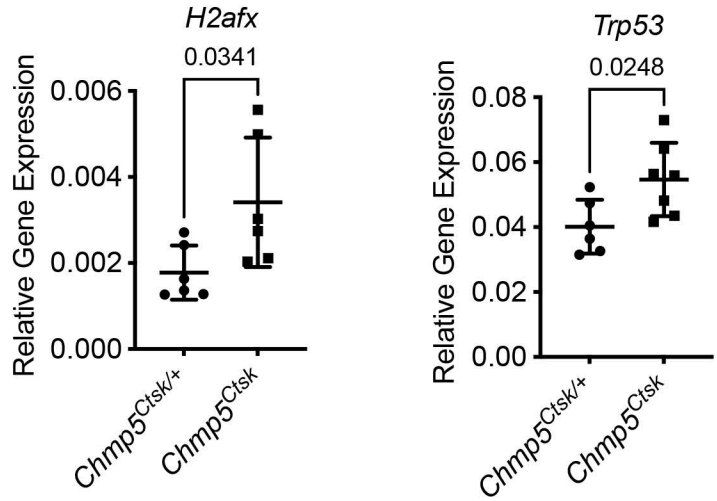
H2afx
0.0341
Trp53
0.0248
Relative Gene Expression
Chmp5Ctsk/+
Chmp5Ctsk